$p62^{(tg/+)}$ mice ($p < 0.05$; Fig. 6*H*). An increase in p62 also significantly increased the survival rate of AR–97Q/$p62^{(tg/+)}$ mice compared with AR–97Q/$p62^{(+/+)}$ mice ($p = 0.008$; Fig. 6*I*). Although the AR–97Q/$p62^{(tg/+)}$ mice took relatively shorter steps than the wild-type mice, they walked with significantly longer steps than the AR–97Q/$p62^{(+/+)}$ mice ($p < 0.01$; Fig. 6*J*).

p62 overexpression promotes NI body formation and reduces DNS of mutant AR in an SBMA mouse model

We performed immunohistochemical staining for mutant AR using the 1C2 antibody in the spinal cord and skeletal muscle of 25-week-old mice. Intriguingly, numerous NIs of the mutant AR were observed in AR–97Q/$p62^{(tg/+)}$ mice but not in AR–97Q/$p62^{(+/+)}$ mice (Fig. 7*A*). The intensity of the DNS was reduced in cells with NIs (Fig. 7*A*, arrow) compared with cells without NIs (Fig. 7*A*, arrowhead). The ratio of the number of cells with NIs to the number of total 1C2-positive cells significantly increased in AR–97Q/$p62^{(tg/+)}$ mice (Fig. 7*B*), and the number of cells with DNS was significantly decreased in AR–97Q/$p62^{(tg/+)}$ mice (Fig. 7*C*). The R.S.I. of the DNS was significantly reduced in cells with NIs compared with those without NIs in the spinal anterior horn and skeletal muscle (Fig. 7*D*). We evaluated the colocalization of overexpressed human p62 and mutant AR in AR–97Q/$p62^{(tg/+)}$ mice. Intriguingly, double-immunofluorescence staining with anti-HA and 1C2 antibodies and immunohistochemistry with an anti-HA antibody demonstrated that p62–HA and mutant AR colocalized in all of the NIs but not in the DNS in the spinal anterior horn cells and skeletal muscles of AR–97Q mice (Fig. 7*E–H*). In addition, p62 localized in the core of NIs of mutant AR (Fig. 7*I*). Double-immunofluorescence staining with anti-p62 and 1C2 antibodies also revealed that endogenous p62 and mutant AR colocalized in the NIs in the spinal anterior horn cells and skeletal muscles of AR–97Q mice (Fig. 8*A*,*B*) and in the spinal anterior horn neurons of human SBMA patients (Fig. 8*C*,*D*), which suggests that endogenous p62 coexists with mutant AR and can exert a cell-protective function in both AR–97Q mice and SBMA patients. There were no NIs in the spinal cord and skeletal muscle of the AR–24Q/$p62^{(tg/+)}$ mice (data not shown).

p62 overexpression reduces the monomeric and oligomeric protein expression of mutant AR in an SBMA mouse model

Overexpression of p62 significantly decreased the amount of the high-molecular-weight mutant AR protein complex and the monomeric form of the mutant AR (AR–97Q) in the spinal cord and skeletal muscle of AR–97Q mice, whereas it did not decrease the expression of wild-type monomeric AR (AR–24Q) (Fig. 9*A*,*B*). To address whether nuclear ARs shift from a more soluble oligomer to a less soluble and aggregated state in AR–97Q/$p62^{(tg/+)}$ mice, we lysed the pellet in 8 M urea solution and performed Western blotting. Overexpression of p62 significantly increased AR protein in the pellet of the spinal cord and skeletal muscle of AR–97Q/$p62^{(tg/+)}$ mice, suggesting that increasing p62 shifts from soluble oligomeric AR to insoluble AR (Fig. 9*C*,*D*). The respective levels of wild-type and mutant AR mRNA were similar in AR–24Q and AR–97Q mice overexpressing p62 (Fig. 9*E*). Anti-GFAP staining showed an apparent decrease in reactive astrogliosis in AR–97Q/$p62^{(tg/+)}$ mice when compared with AR–97Q/$p62^{(+/+)}$ mice in the spinal anterior horn (Fig. 9*F*,*G*). Western blotting analyses with an antibody against GFAP revealed that overexpression of p62 downregulated GFAP, which indicates that the overexpression of p62 mitigated the neurodegenerative changes (Fig. 9*H*). Muscle histology and weight measurements also demonstrated a significant amelioration of muscle atrophy in AR–97Q/$p62^{(tg/+)}$ mice compared with AR–97Q/$p62^{(+/+)}$ mice (Fig. 9*I*,*J*). The AR–97Q/$p62^{(tg/+)}$ muscles were 2.2 times heavier than the AR–97Q/$p62^{(+/+)}$ muscles (Fig. 9*K*). Overexpression of p62 did not influence the expression of the total amount of ubiquitinated proteins in the spinal cord and muscle of AR–24Q and AR–97Q mice, as determined by Western blots (Fig. 9*L*), whereas more ubiquitin-positive NIs were identified in the AR–97Q/$p62^{(tg/+)}$ mice than in the AR–97Q/$p62^{(+/+)}$ mice (Fig. 9*M*,*N*). The expression of the autophagic marker LC3 (Mizushima et al., 2010) was slightly elevated in the spinal cord and muscle of AR–24Q/$p62^{(tg/+)}$ and AR–97Q/$p62^{(tg/+)}$ mice compared with AR–24Q/$p62^{(+/+)}$ and AR–97Q/$p62^{(+/+)}$ mice (Fig. 10*A*,*B*), which suggests that high expression of p62 induced autophagosome formation to some extent. However, the induction of autophagosome formation could be insufficient to affect the degradation of the AR protein because p62 overexpression did not decrease the expression of wild-type AR in the spinal cord and skeletal muscle of AR–24Q mice (Fig. 9*A*,*B*). Overexpression of p62 did not influence the expression of wild-type and mutant AR in two SBMA cellular models (Fig. 11*A*,*B*). In this culture system, we detected a band that represented a monomeric mutant AR in the separating gel. However, it was difficult to detect the high-molecular-weight mutant AR protein complex and NIs. Thus, this cell culture model is more appropriate for estimating changes in monomeric mutant AR expression. These observations suggest that an increase in p62 promotes the downregulation of soluble-toxic mutant AR species via harmless inclusion body formation rather than by autophagic degradation and exerts therapeutic effects in AR–97Q mice. Our results were consistent with those of a previous study that showed that NI formation exhibits protective effects in a cellular model of Huntington's disease (Arrasate et al., 2004).

Discussion

The protein p62 is a ubiquitously expressed cellular protein, and it has been shown recently to be a selective substrate for autophagy (Bjørkøy et al., 2005; Pankiv et al., 2007; Ichimura et al., 2008). This protein is localized at the autophagosome formation site (Itakura and Mizushima, 2011) and directly interacts with LC3, which is an autophagosome-localizing protein (Pankiv et al., 2007; Ichimura et al., 2008). Subsequently, p62 incorporates into the autophagosome and is then degraded (Pankiv et al., 2007; Ichimura et al., 2008). Thus, impaired autophagy is accompanied by the accumulation of p62, followed by the formation of p62- and ubiquitin-positive aggregates because of the nature of self-oligomerization and ubiquitin binding by p62 (Mizushima and Komatsu, 2011). In contrast, inclusion bodies that are positive for both ubiquitin and p62 have been identified in various neurodegenerative disorders (Kuusisto et al., 2001,

←

(*Figure legend continued.*) Bars represent the density of 1C2-positive cells in AR–97Q/$p62^{+/+}$, AR–97Q/$p62^{+/-}$, and AR–97Q/$p62^{-/-}$ mice. The results are expressed as the means ± SEM ($n = 6$). ***I***, ***J***, Western blotting analysis of the total tissue homogenates from the spinal cord (***I***) and muscle (***J***) of AR–24Q and AR–97Q mice (13 weeks of age, $n = 6$), probed with anti-AR. Values are expressed as the means ± SEM ($n = 6$). ***K***, ***L***, Immunohistochemical staining with anti-GFAP antibody in the spinal anterior horn. Scale bars, 30 μm. ***M***, Western blotting analysis of the total tissue homogenates from the spinal cord of AR–97Q mice (13 weeks of age, $n = 6$) probed with anti-GFAP. ***N***, ***O***, Hematoxylin and eosin staining of the muscles. ***P***, The gastrocnemius muscles from AR–97Q/$p62^{+/+}$ and AR–97Q/$p62^{-/-}$ mice were dissected and weighed. ***Q***, Western blotting analysis of the total tissue homogenates from the spinal cord and muscle of AR–24Q and AR–97Q mice (13 weeks of age) probed with anti-ubiquitin (Ub). Scale bars, 50 μm. $^*p < 0.05$; $^{**}p < 0.01$; $^{***}p < 0.001$.

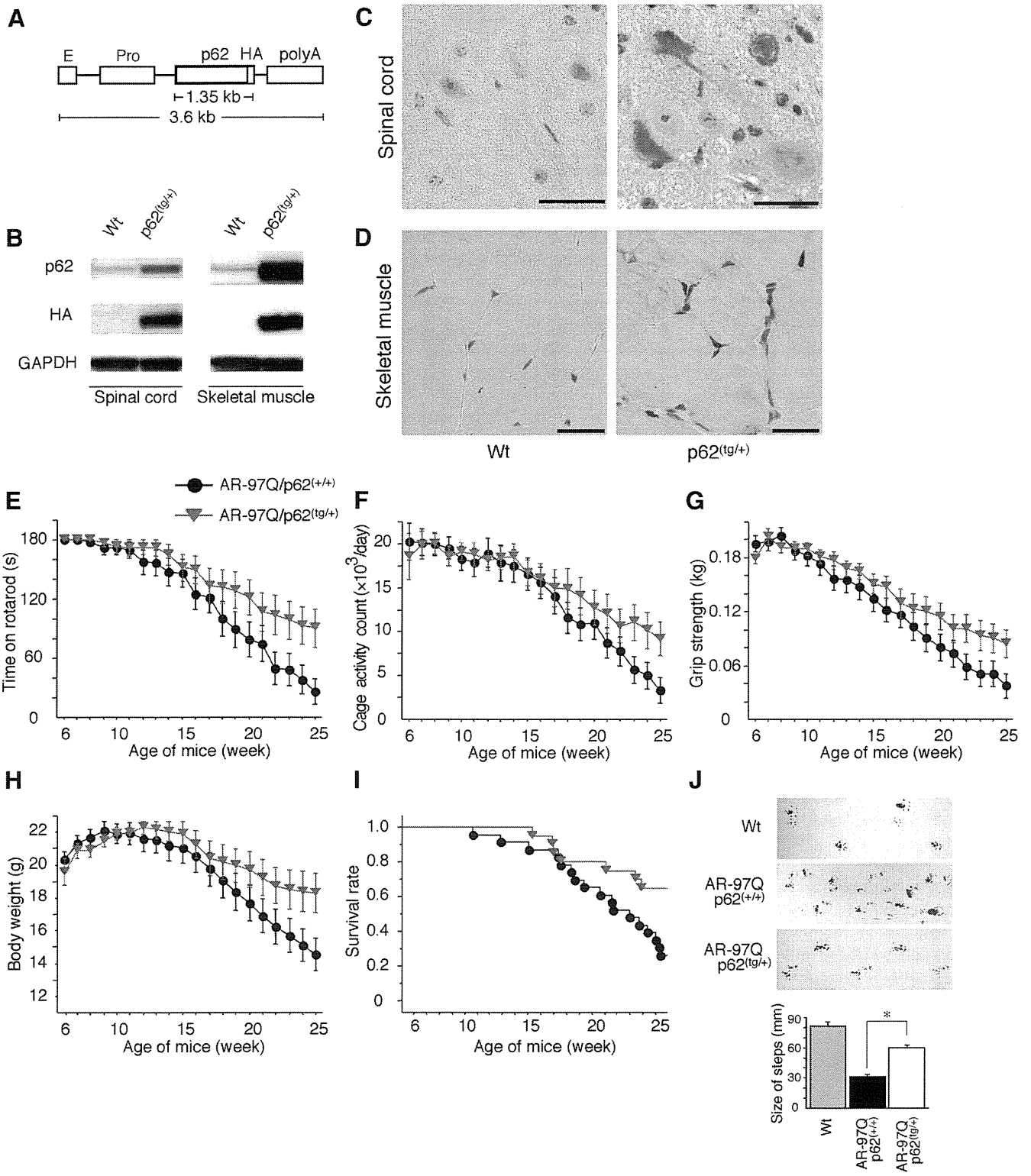

Figure 6. p62 overexpression ameliorates behavioral and visible phenotypes in male AR–97Q mice. ***A***, A schematic view of the transgene construct. The microinjected fragment was composed of a cytomegalovirus enhancer (***E***), a chicken β-actin promoter (Pro), full-length human p62 with an HA tag, and a rabbit β-globin polyadenylation signal sequence (polyA). ***B***, Western blotting analysis of total spinal cord and muscle protein lysates from wild-type (Wt) and $p62^{(tg/+)}$ mice immunolabeled with antibodies against p62 and HA. ***C***, ***D***, HA immunohistochemistry in the spinal anterior horn (***C***) and skeletal muscle (***D***) of 13-week-old wild-type (Wt) and $p62^{(tg/+)}$ mice counterstained with Mayer's hematoxylin. p62 immunoreactivity localized to the nuclei and cytoplasms of anterior horn cells (***C***) and skeletal muscle (***D***). HA staining was absent in the wild-type mice. Scale bars, 50 μm. ***E–I***, Rotarod task (***E***), cage activity (***F***), grip strength (***G***), body weight (***H***), and survival rate (***I***) of AR–97Q/$p62^{(+/+)}$ (●; $n = 25$) and AR–97Q/$p62^{(tg/+)}$(▼; $n = 21$) mice. ***J***, Footprints of representative 25-week-old AR–97Q/$p62^{(+/+)}$ and AR–97Q/$p62^{(tg/+)}$ mice. The front paws are indicated in blue, and the hindpaws are indicated in red. Values are expressed as the means ± SEM. *$p < 0.01$.

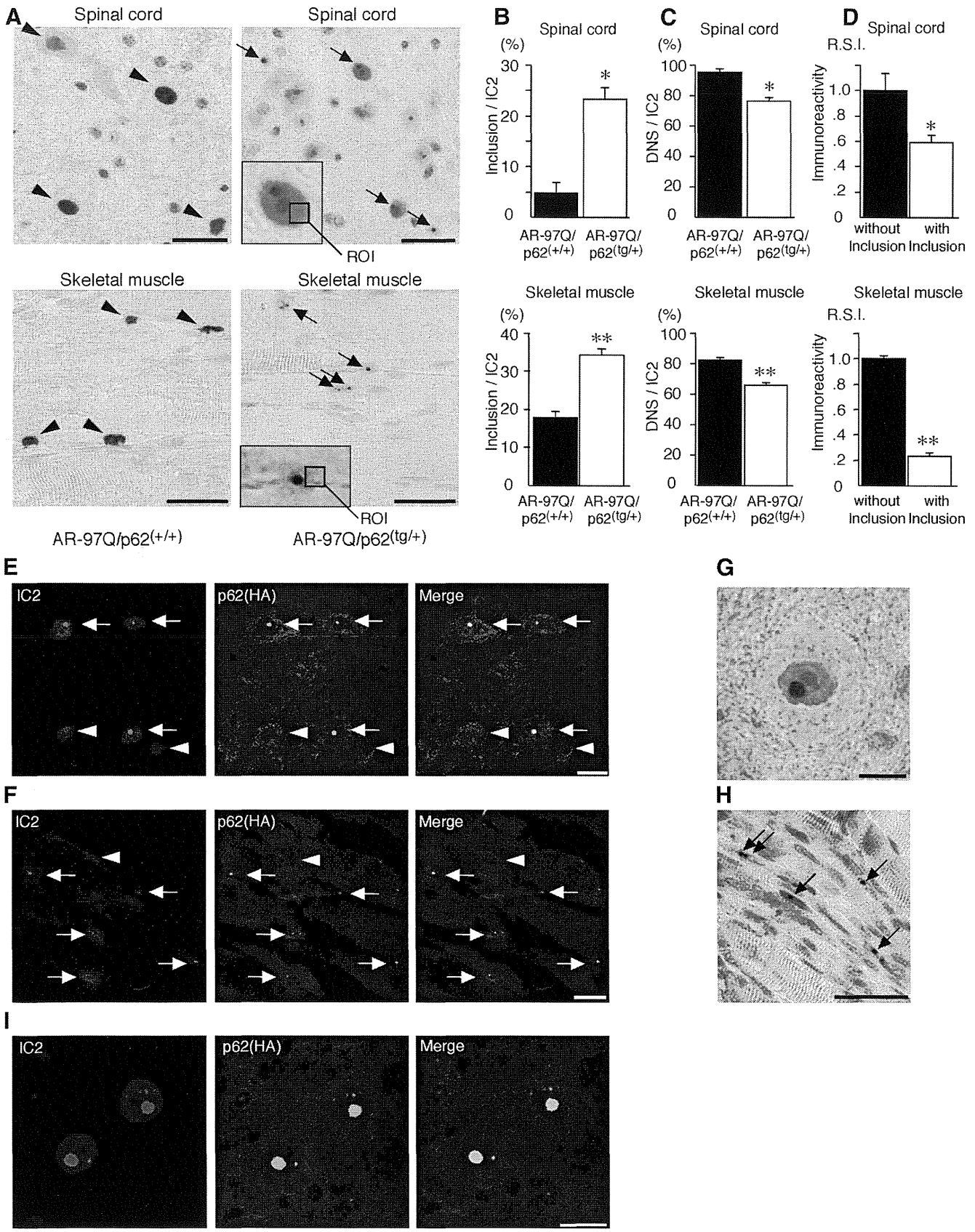

Figure 7. p62 promotes inclusion body formation of ARs in male AR–97Q mice. ***A***, Immunohistochemical staining with 1C2 antibody revealed DNS (arrowhead) in AR–97Q/*p62*$^{(+/+)}$ mice and many NIs (arrow) in the AR–97Q/*p62*$^{(tg/+)}$ mice in the spinal anterior horn and skeletal muscle at 25 weeks of age. The region of interest for the DNS is defined as the ROI (inset; open square). Scale bars, 30 μm. ***B***, The ratio of the number of cells with NIs to the total number of IC2-positive cells. ***C***, The ratio of the number of cells with DNS to the total number of IC2-positive cells. ***D***, The R.S.I. of the DNS was significantly reduced in cells with NIs compared with those without NIs in spinal anterior horn neurons and skeletal muscle. ***E***, ***F***, Double-immunofluorescence staining with 1C2 (red) and anti-HA (green) antibodies in the spinal anterior horn (***E***) and skeletal muscle (***F***) of AR–97Q/*p62*$^{(tg/+)}$ mice revealed the complete colocalization of HA-tagged p62 and (*Figure legend continues.*)

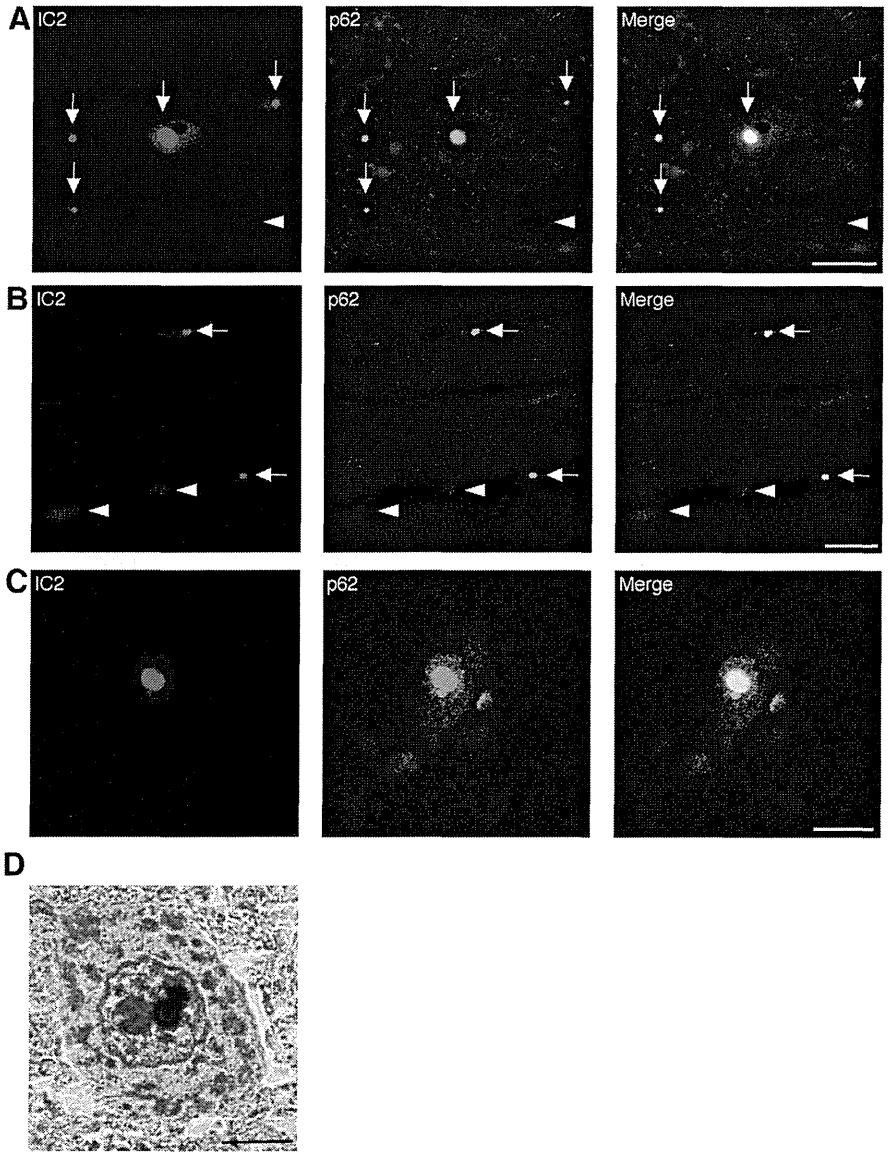

Figure 8. Colocalization of nuclear-localized p62 with mutant AR. ***A–C***, 1C2 (red) and anti-HA (green) double immunofluorescence in the spinal cord (***A***) and skeletal muscle (***B***) of 16-week-old AR–97Q mice and in the spinal anterior horn cells (***C***) of SBMA patients. Double-immunofluorescence staining revealed p62 and mutant AR colocalization in NIs (shown in yellow, arrow), but no colocalization was observed in the DNS (arrowhead) in AR–97Q mice and SBMA patients. Scale bars, 20 μm. ***D***, Immunohistochemistry for the anti-p62 antibody in SBMA patients. p62 was localized in the NIs. Scale bar, 10 μm.

2008), which suggests that p62 contributes to inclusion formation. Furthermore, p62-positive aggregates observed in hepatocytes and neurons of liver- and brain-specific Atg7-deficient mice are completely dispersed by the additional loss of p62 (Komatsu et al., 2007).

We generated an SBMA transgenic mouse model (AR–97Q) that displayed progressive muscular atrophy, weakness, and DNS and NIs of the mutant AR in neuronal and non-neuronal tissues (Katsuno et al., 2002). Because AR has a specific ligand (i.e., testosterone), the pathogenesis of SBMA is unique among the polyQ diseases (Katsuno et al., 2003). The success of androgen deprivation therapy in SBMA mouse models has been translated into clinical trials (Katsuno et al., 2010; Fernández-Rhodes et al., 2011). In addition, the elucidation of SBMA pathophysiology using animal models has led to the development of other therapeutics, including chaperone-related disease-modifying therapy (Waza et al., 2005; Tokui et al., 2009), posttranslational modification of the AR (Palazzolo et al., 2009; Montie et al., 2011), AR mRNA stability (Miyazaki et al., 2012), and modulation of the NH_2–/carboxyl-terminal interaction of the AR (Orr et al., 2010), which inhibit the pathogenic process of neuronal degeneration. Thus, there is increasing evidence that AR ligands, molecular chaperones–UPS, and autophagy play crucial roles in the pathogenesis of SBMA. Furthermore, mutant AR that bears an expanded polyQ repeat adopts an altered conformation that results in protein aggregation and inclusion formation; however, recent studies have suggested that soluble causative protein species that include protein aggregates, rather than protein inclusions, could be toxic; thus, they represent targets in the treatment of neurodegenerative disorders (Bauer and Nukina, 2009; Naiki and Nagai, 2009; Hands and Wyttenbach, 2010). In this study, we addressed the questions of whether depletion of p62 exacerbates neuropathological outcomes and whether overexpression of p62 can protect against mutant AR toxicity and exert therapeutic effects on the SBMA phenotype. Depletion of p62 significantly increased the accumulation of monomeric mutant AR and mutant AR protein complexes in AR–97Q mice via an impairment of autophagic degradation, whereas helpful inclusion body formation was promoted in the spinal cord and muscle of the AR–97Q/p62 double transgenic mice.

In a neuronal cell culture model of SBMA, we demonstrated that decreasing levels of p62 inhibited the degradation of monomeric wild-type and mutant ARs even in cells with NIs, which suggests that p62 plays a pivotal role in AR protein turnover. Growing evidence indicates that p62, together with ubiquitinated proteins, is transported into autophagosomes, which suggests that p62 is a receptor for ubiquitinated proteins that is necessary for their degradation in lysosomes (Johansen and Lamark, 2011). As a receptor, p62 would also contribute to autophagic degradation of Parkin-mediated ubiquitinated mitochondria (Geisler et al., 2010). Furthermore, p62 is localized at the autophagosome formation site and directly interacts with LC3, which facilitates the delivery of its polyubiquitinated protein for lysosomal degradation (Ichimura et al., 2008). Subsequently, p62 is also incorporated into the autophagosome and is then degraded. In addition,

←

(*Figure legend continued.*) mutant AR in NIs (arrow), but no colocalization was observed in the DNS (arrowhead). Scale bars, 20 μm. ***G***, ***H***, p62 immunohistochemistry in the spinal anterior horn neurons (***G***) and skeletal muscle (***H***) of AR–97Q/$p62^{(tg/+)}$ mice. Arrows indicate NIs. Scale bars: ***G***, 30 μm; ***H***, 50 μm. Values are expressed as the means ± SEM ($n = 6$). ***I***, 1C2 (red) and anti-HA (green) double immunofluorescence in the spinal cord of 25-week-old AR–97Q/$p62^{(tg/+)}$ mice. *$p < 0.01$; **$p < 0.001$.

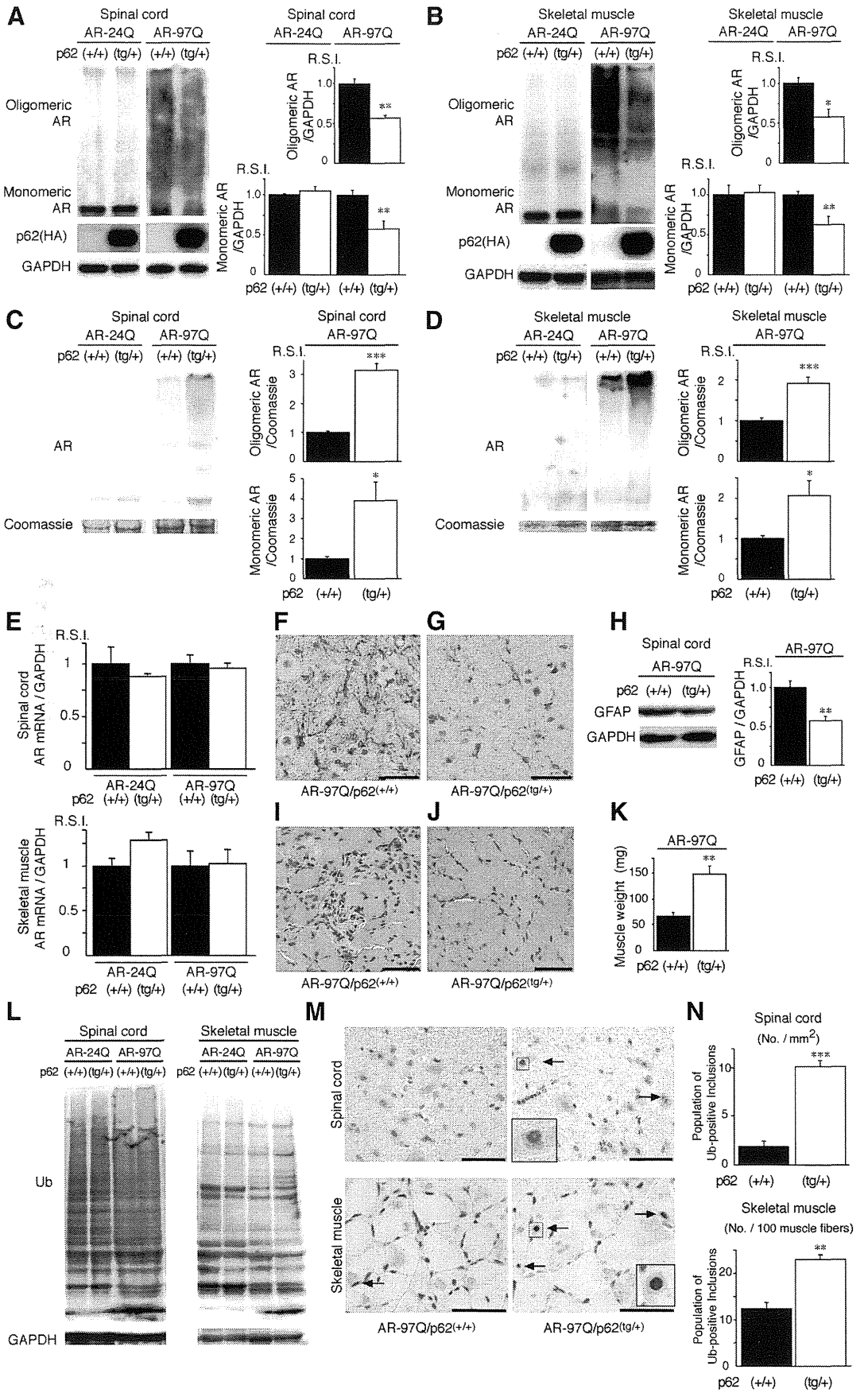

Figure 9. An increase in p62 reduces mutant AR expression. ***A***, ***B***, Western blotting analysis of total tissue homogenates from the spinal cord (***A***) and muscle (***B***) of AR–24Q and AR–97Q mice (25 weeks of age) probed with anti-AR. Values are expressed as the means ± SEM ($n = 5$). ***C***, ***D***, Western blotting analysis of the pellet lysed in 8 M urea solution from the spinal (*Figure legend continues.*)

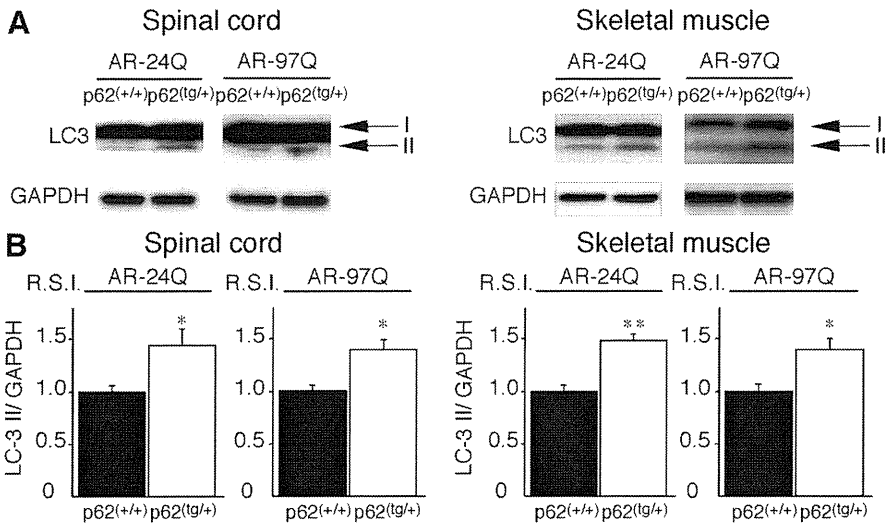

Figure 10. LC3-II expression in AR–97Q/$p62^{(tg/+)}$ mice. ***A***, Western blotting analysis of total spinal cord protein lysates from the AR–97Q/$p62^{(+/+)}$ and AR–97Q/$p62^{(tg/+)}$ mice immunolabeled with antibodies against LC3. ***B***, Quantitative analysis for the amounts of LC3-II. LC3-II levels were slightly elevated in the AR–97Q/$p62^{(tg/+)}$ mice. This experiment was repeated in four sets of mice with equivalent results. All of the values are expressed as the means ± SEM ($n = 5$). *$p < 0.05$; **$p < 0.01$.

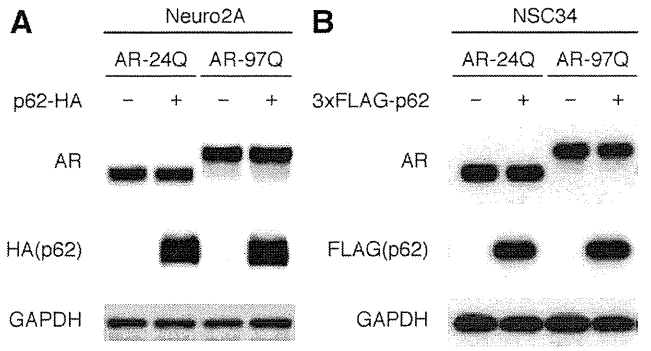

Figure 11. p62 overexpression does not affect AR expression. ***A***, Full-length wild-type (24Q) or mutant (97Q) AR and HA-tagged p62 (pCAGGS–p62–HA) were cotransfected into Neuro2A cells for 48 h. ***B***, Full-length wild-type (24Q) or mutant (97Q) AR and FLAG-tagged p62 (pIRES-puro3–3XFLAG–p62) were cotransfected into NSC34 cells for 48 h. All of the cells were cultured in DMEM/10% FCS at 37°C and with 5% CO_2. Immunoblots revealed that the expression of AR was similar in the presence or absence of HA–p62 or FLAG–p62.

p62 has been shown to directly interact with mutant copper–zinc superoxide dismutase (SOD1) protein (Gal et al., 2007), which indicates that p62 directly or indirectly recognizes the mutant SOD1 protein and is degraded via autophagy. p62 also has the capacity to sequester aggregate-prone proteins that might otherwise undergo proteasomal degradation (Korolchuk et al., 2009). In our study, both wild-type and mutant ARs colocalized with endogenous p62- and LC3-positive puncta (Fig. 1*C*). In addition, ARs were recognized directly by p62 (Fig. 2), which suggests that mutant AR is degraded in a p62-dependent autophagic pathway. Furthermore, our Western blotting analysis revealed that monomeric mutant AR and the high-molecular-weight form of mutant AR protein complexes retained in the stacking gel were upregulated in the spinal cord and muscle of AR–97Q transgenic/p62 knock-out mice, which suggests that degradation of mutant AR was inhibited by the deletion of p62.

In addition, the overexpression of p62 did not influence the expression of wild-type and mutant AR in a cellular model of SBMA or the expression of wild-type AR in a transgenic mouse model, which suggests that p62 overexpression was not sufficient to promote the degradation of both wild-type and mutant AR (Figs. 9*A*,*B*, 11*A*,*B*). However, p62 overexpression enhanced the inclusion body formation of mutant ARs, which resulted in a reduction of expression in a transgenic mouse model (Figs. 7, 9), and this effect can occur independently of the degradation in lysosomes. More importantly, overexpressed p62 existed in all of the mutant AR NIs in the spinal cord and skeletal muscle of AR–97Q/p62 double transgenic mice. Furthermore, p62 also colocalized with mutant AR NIs that were present in the anterior horn cells of postmortem tissues obtained from SBMA patients. Inclusion bodies that were positive for both ubiquitin and p62 have been identified in various neurodegenerative diseases, which suggests that p62 is involved in the formation of disease-related inclusion bodies (Kuusisto et al., 2001, 2008; Labbadia et al., 2012). Intriguingly, the overexpressed p62 and mutant AR colocalized in all of the NIs but not in the DNS, and p62 was localized in the core of NIs of mutant AR (Fig. 7*I*). p62 can either directly or indirectly interact with the AR without its ubiquitination (Fig. 2*G*) and can also function with the misfolded AR, as indicated by the fact that we did not observe NI formation in the AR–24Q/ $p62^{(tg/+)}$ mice. These results suggest that p62 is capable of self-oligomerization and could provide an opportunity for inclusion formation to generate the seeds of NIs.

However, the extent of diffuse nuclear accumulation of mutant AR in motor and sensory neurons of the spinal cord of autopsied SBMA patients was strongly correlated with the CAG repeat length but not with the number of NIs (Adachi et al., 2005). Accumulating evidence suggests that NIs are not harmful polyQ species (Arrasate et al., 2004) and instead that an oligomeric form of the mutant protein could be the major pathogenic species (Nagai et al., 2007; Sathasivam et al., 2010). Several studies have suggested that inclusion formation could be a cellular response against the toxicity of abnormal polyQ proteins (Arrasate et al., 2004; Bowman et al., 2005), whereas the nuclear localization or accumulation of abnormal proteins can be decisive in inducing neuronal cell dysfunction and degeneration in polyQ diseases, including SBMA (Klement et al., 1998; Saudou et al., 1998; Adachi et al., 2005). In view of the time course of SBMA,

←

(*Figure legend continued.*) cord (***C***) and muscle (***D***) of AR–24Q and AR–97Q mice (25 weeks of age) probed with anti-AR. Values are expressed as the means ± SEM ($n = 5$). ***E***, Real-time RT-PCR of wild-type and mutant AR mRNA normalized to GAPDH levels. ***F***, ***G***, Immunohistochemical staining with anti-GFAP antibody in the spinal anterior horn. Scale bars, 30 μm. ***H***, Western blotting analysis of the total tissue homogenates from the spinal cord of AR–97Q mice (25 weeks of age, $n = 5$) probed with anti-GFAP. ***I***, ***J***, Hematoxylin and eosin staining of the muscle. Scale bars, 50 μm. ***K***, The gastrocnemius muscles from AR–97Q/$p62^{(+/+)}$ and AR–97Q/$p62^{(tg/+)}$ mice were dissected and weighed. ***L***, Western blotting analysis of the total tissue homogenates from the spinal cord and muscle of AR–24Q and AR–97Q mice (25 weeks of age) probed with anti-ubiquitin (Ub). ***M***, Ubiquitin immunohistochemistry revealed NIs (arrow) in the spinal anterior horn and muscle of 25-week-old AR–97Q/$p62^{(+/+)}$ and AR–97Q/$p62^{(tg/+)}$ mice. The inset shows a magnified image in the square box. Scale bars, 50 μm. ***N***, Quantitative assessment of ubiquitin-positive NIs in the spinal ventral horn and muscle. Bars represent the density of ubiquitin-positive NIs in AR–97Q/$p62^{(+/+)}$ and AR–97Q/$p62^{(tg/+)}$ mice. The results are expressed as the means ± SEM ($n = 6$). *$p < 0.05$; **$p < 0.01$; ***$p < 0.001$.

diffuse nuclear accumulation of mutant proteins with an expanded polyQ tract might be an early event that occurs before NI formation, which is closely related to the manifestation of neuronal dysfunction (Watase et al., 2002; Yoo et al., 2003). The molecular pathogenetic process by which diffuse nuclear mutant AR accumulation induces neuronal dysfunction and death remains unclear; however, it is notable that overexpression of p62 can promote NI formation and the packaging of accumulated soluble and toxic nuclear mutant AR.

Accumulation of misfolded proteins is causally related to many age-related neurodegenerative diseases (Bates, 2006). Prompt removal and/or refolding could be required more in aged or damaged cells than in young healthy cells, in which protein quality control systems function appropriately. In SBMA patients, diffuse nuclear accumulation of mutant AR is frequent and extensive, and it occurs in a wide array of CNS nuclei and visceral organs. The precise mechanism used by the mutant protein must be determined in future studies; however, we have used cellular and mouse models of SBMA and demonstrated that p62 plays a beneficial role in autophagic degradation and NI formation of the mutant AR protein. These findings provide new insights into the cytoprotective functions of p62; thus, they could have important implications for the development of therapeutic strategies for the treatment of SBMA and other polyQ diseases.

References

Adachi H, Kume A, Li M, Nakagomi Y, Niwa H, Do J, Sang C, Kobayashi Y, Doyu M, Sobue G (2001) Transgenic mice with an expanded CAG repeat controlled by the human AR promoter show polyglutamine nuclear inclusions and neuronal dysfunction without neuronal cell death. Hum Mol Genet 10:1039–1048. CrossRef Medline

Adachi H, Katsuno M, Minamiyama M, Waza M, Sang C, Nakagomi Y, Kobayashi Y, Tanaka F, Doyu M, Inukai A, Yoshida M, Hashizume Y, Sobue G (2005) Widespread nuclear and cytoplasmic accumulation of mutant androgen receptor in SBMA patients. Brain 128:659–670. CrossRef Medline

Adachi H, Waza M, Katsuno M, Tanaka F, Doyu M, Sobue G (2007) Pathogenesis and molecular targeted therapy of spinal and bulbar muscular atrophy. Neuropathol Appl Neurobiol 33:135–151. CrossRef Medline

Adachi H, Katsuno M, Waza M, Minamiyama M, Tanaka F, Sobue G (2009) Heat shock proteins in neurodegenerative diseases: pathogenic roles and therapeutic implications. Int J Hyperthermia 25:647–654. CrossRef Medline

Al-Sarraj S, King A, Troakes C, Smith B, Maekawa S, Bodi I, Rogelj B, Al-Chalabi A, Hortobágyi T, Shaw CE (2011) p62 positive, TDP-43 negative, neuronal cytoplasmic and intranuclear inclusions in the cerebellum and hippocampus define the pathology of C9orf72-linked FTLD and MND/ALS. Acta Neuropathol 122:691–702. CrossRef Medline

Arrasate M, Mitra S, Schweitzer ES, Segal MR, Finkbeiner S (2004) Inclusion body formation reduces levels of mutant huntingtin and the risk of neuronal death. Nature 431:805–810. CrossRef Medline

Bailey CK, Andriola IF, Kampinga HH, Merry DE (2002) Molecular chaperones enhance the degradation of expanded polyglutamine repeat androgen receptor in a cellular model of spinal and bulbar muscular atrophy. Hum Mol Genet 11:515–523. CrossRef Medline

Bates GP (2006) BIOMEDICINE: one misfolded protein allows others to sneak by. Science 311:1385–1386. CrossRef Medline

Bauer PO, Nukina N (2009) The pathogenic mechanisms of polyglutamine diseases and current therapeutic strategies. J Neurochem 110:1737–1765. CrossRef Medline

Bjørkøy G, Lamark T, Brech A, Outzen H, Perander M, Overvatn A, Stenmark H, Johansen T (2005) p62/SQSTM1 forms protein aggregates degraded by autophagy and has a protective effect on huntingtin-induced cell death. J Cell Biol 171:603–614. CrossRef Medline

Bowman AB, Yoo SY, Dantuma NP, Zoghbi HY (2005) Neuronal dysfunction in a polyglutamine disease model occurs in the absence of ubiquitin-proteasome system impairment and inversely correlates with the degree of nuclear inclusion formation. Hum Mol Genet 14:679–691. CrossRef Medline

Buchberger A, Bukau B, Sommer T (2010) Protein quality control in the cytosol and the endoplasmic reticulum: brothers in arms. Mol Cell 40:238–252. CrossRef Medline

Di Prospero NA, Fischbeck KH (2005) Therapeutics development for triplet repeat expansion diseases. Nat Rev Genet 6:756–765. CrossRef Medline

Falchetti A, Di Stefano M, Marini F, Del Monte F, Mavilia C, Strigoli D, De Feo ML, Isaia G, Masi L, Amedei A, Cioppi F, Ghinoi V, Bongi SM, Di Fede G, Sferrazza C, Rini GB, Melchiorre D, Matucci-Cerinic M, Brandi ML (2004) Two novel mutations at exon 8 of the Sequestosome 1 (SQSTM1) gene in an Italian series of patients affected by Paget's disease of bone (PDB). J Bone Miner Res 19:1013–1017. CrossRef Medline

Fernández-Rhodes LE, Kokkinis AD, White MJ, Watts CA, Auh S, Jeffries NO, Shrader JA, Lehky TJ, Li L, Ryder JE, Levy EW, Solomon BI, Harris-Love MO, La Pean A, Schindler AB, Chen C, Di Prospero NA, Fischbeck KH (2011) Efficacy and safety of dutasteride in patients with spinal and bulbar muscular atrophy: a randomised placebo-controlled trial. Lancet Neurol 10:140–147. CrossRef Medline

Gal J, Ström AL, Kilty R, Zhang F, Zhu H (2007) p62 accumulates and enhances aggregate formation in model systems of familial amyotrophic lateral sclerosis. J Biol Chem 282:11068–11077. CrossRef Medline

Geisler S, Holmström KM, Skujat D, Fiesel FC, Rothfuss OC, Kahle PJ, Springer W (2010) PINK1/Parkin-mediated mitophagy is dependent on VDAC1 and p62/SQSTM1. Nat Cell Biol 12:119–131. CrossRef Medline

Hands SL, Wyttenbach A (2010) Neurotoxic protein oligomerisation associated with polyglutamine diseases. Acta Neuropathol 120:419–437. CrossRef Medline

Ichimura Y, Komatsu M (2010) Selective degradation of p62 by autophagy. Semin Immunopathol 32:431–436. CrossRef Medline

Ichimura Y, Kumanomidou T, Sou YS, Mizushima T, Ezaki J, Ueno T, Kominami E, Yamane T, Tanaka K, Komatsu M (2008) Structural basis for sorting mechanism of p62 in selective autophagy. J Biol Chem 283:22847–22857. CrossRef Medline

Itakura E, Mizushima N (2011) p62 Targeting to the autophagosome formation site requires self-oligomerization but not LC3 binding. J Cell Biol 192:17–27. CrossRef Medline

Johansen T, Lamark T (2011) Selective autophagy mediated by autophagic adapter proteins. Autophagy 7:279–296. CrossRef Medline

Katsuno M, Banno H, Suzuki K, Takeuchi Y, Kawashima M, Yabe I, Sasaki H, Aoki M, Morita M, Nakano I, Kanai K, Ito S, Ishikawa K, Mizusawa H, Yamamoto T, Tsuji S, Hasegawa K, Shimohata T, Nishizawa M, Miyajima H, et al. (2010) Efficacy and safety of leuprorelin in patients with spinal and bulbar muscular atrophy (JASMITT study): a multicentre, randomised, double-blind, placebo-controlled trial. Lancet Neurol 9:875–884. CrossRef Medline

Katsuno M, Adachi H, Kume A, Li M, Nakagomi Y, Niwa H, Sang C, Kobayashi Y, Doyu M, Sobue G (2002) Testosterone reduction prevents phenotypic expression in a transgenic mouse model of spinal and bulbar muscular atrophy. Neuron 35:843–854. CrossRef Medline

Katsuno M, Adachi H, Doyu M, Minamiyama M, Sang C, Kobayashi Y, Inukai A, Sobue G (2003) Leuprorelin rescues polyglutamine-dependent phenotypes in a transgenic mouse model of spinal and bulbar muscular atrophy. Nat Med 9:768–773. CrossRef Medline

King A, Maekawa S, Bodi I, Troakes C, Al-Sarraj S (2011) Ubiquitinated, p62 immunopositive cerebellar cortical neuronal inclusions are evident across the spectrum of TDP-43 proteinopathies but are only rarely additionally immunopositive for phosphorylation-dependent TDP-43. Neuropathology 31:239–249. CrossRef Medline

Klement IA, Skinner PJ, Kaytor MD, Yi H, Hersch SM, Clark HB, Zoghbi HY, Orr HT (1998) Ataxin-1 nuclear localization and aggregation: role in polyglutamine-induced disease in SCA1 transgenic mice. Cell 95:41–53. CrossRef Medline

Komatsu M, Waguri S, Koike M, Sou YS, Ueno T, Hara T, Mizushima N, Iwata J, Ezaki J, Murata S, Hamazaki J, Nishito Y, Iemura S, Natsume T, Yanagawa T, Uwayama J, Warabi E, Yoshida H, Ishii T, Kobayashi A, et al. (2007) Homeostatic levels of p62 control cytoplasmic inclusion body formation in autophagy-deficient mice. Cell 131:1149–1163. CrossRef Medline

Korolchuk VI, Mansilla A, Menzies FM, Rubinsztein DC (2009) Autophagy inhibition compromises degradation of ubiquitin-proteasome pathway substrates. Mol Cell 33:517–527. CrossRef Medline

Kuusisto E, Salminen A, Alafuzoff I (2001) Ubiquitin-binding protein p62 is

present in neuronal and glial inclusions in human tauopathies and synucleinopathies. Neuroreport 12:2085–2090. CrossRef Medline

Kuusisto E, Kauppinen T, Alafuzoff I (2008) Use of p62/SQSTM1 antibodies for neuropathological diagnosis. Neuropathol Appl Neurobiol 34: 169–180. CrossRef Medline

Labbadia J, Cunliffe H, Weiss A, Katsyuba E, Sathasivam K, Seredenina T, Woodman B, Moussaoui S, Frentzel S, Luthi-Carter R, Paganetti P, Bates GP (2011) Altered chromatin architecture underlies progressive impairment of the heat shock response in mouse models of Huntington disease. J Clin Invest 121:3306–3319. CrossRef Medline

Labbadia J, Novoselov SS, Bett JS, Weiss A, Paganetti P, Bates GP, Cheetham ME (2012) Suppression of protein aggregation by chaperone modification of high molecular weight complexes. Brain 135:1180–1196. CrossRef Medline

Lamark T, Perander M, Outzen H, Kristiansen K, Øvervatn A, Michaelsen E, Bjørkøy G, Johansen T (2003) Interaction codes within the family of mammalian Phox and Bem1p domain-containing proteins. J Biol Chem 278:34568–34581. CrossRef Medline

Li M, Miwa S, Kobayashi Y, Merry DE, Yamamoto M, Tanaka F, Doyu M, Hashizume Y, Fischbeck KH, Sobue G (1998) Nuclear inclusions of the androgen receptor protein in spinal and bulbar muscular atrophy. Ann Neurol 44:249–254. CrossRef Medline

Lieberman AP, Harmison G, Strand AD, Olson JM, Fischbeck KH (2002) Altered transcriptional regulation in cells expressing the expanded polyglutamine androgen receptor. Hum Mol Genet 11:1967–1976. CrossRef Medline

Matsumoto G, Wada K, Okuno M, Kurosawa M, Nukina N (2011) Serine 403 phosphorylation of p62/SQSTM1 regulates selective autophagic clearance of ubiquitinated proteins. Mol Cell 44:279–289. CrossRef Medline

Miyazaki Y, Adachi H, Katsuno M, Minamiyama M, Jiang YM, Huang Z, Doi H, Matsumoto S, Kondo N, Iida M, Tohnai G, Tanaka F, Muramatsu S, Sobue G (2012) Viral delivery of miR-196a ameliorates the SBMA phenotype via the silencing of CELF2. Nat Med 18:1136–1141. CrossRef Medline

Mizushima N, Komatsu M (2011) Autophagy: renovation of cells and tissues. Cell 147:728–741. CrossRef Medline

Mizushima N, Yoshimori T, Levine B (2010) Methods in mammalian autophagy research. Cell 140:313–326. CrossRef Medline

Montie HL, Cho MS, Holder L, Liu Y, Tsvetkov AS, Finkbeiner S, Merry DE (2009) Cytoplasmic retention of polyglutamine-expanded androgen receptor ameliorates disease via autophagy in a mouse model of spinal and bulbar muscular atrophy. Hum Mol Genet 18:1937–1950. CrossRef Medline

Montie HL, Pestell RG, Merry DE (2011) SIRT1 modulates aggregation and toxicity through deacetylation of the androgen receptor in cell models of SBMA. J Neurosci 31:17425–17436. CrossRef Medline

Nagai Y, Inui T, Popiel HA, Fujikake N, Hasegawa K, Urade Y, Goto Y, Naiki H, Toda T (2007) A toxic monomeric conformer of the polyglutamine protein. Nat Struct Mol Biol 14:332–340. CrossRef Medline

Naiki H, Nagai Y (2009) Molecular pathogenesis of protein misfolding diseases: pathological molecular environments versus quality control systems against misfolded proteins. J Biochem 146:751–756. CrossRef Medline

Niwa H, Yamamura K, Miyazaki J (1991) Efficient selection for high-expression transfectants with a novel eukaryotic vector. Gene 108:193–199. CrossRef Medline

Orr CR, Montie HL, Liu Y, Bolzoni E, Jenkins SC, Wilson EM, Joseph JD, McDonnell DP, Merry DE (2010) An interdomain interaction of the androgen receptor is required for its aggregation and toxicity in spinal and bulbar muscular atrophy. J Biol Chem 285:35567–35577. CrossRef Medline

Palazzolo I, Stack C, Kong L, Musaro A, Adachi H, Katsuno M, Sobue G, Taylor JP, Sumner CJ, Fischbeck KH, Pennuto M (2009) Overexpression of IGF-1 in muscle attenuates disease in a mouse model of spinal and bulbar muscular atrophy. Neuron 63:316–328. CrossRef Medline

Pankiv S, Clausen TH, Lamark T, Brech A, Bruun JA, Outzen H, Øvervatn A, Bjørkøy G, Johansen T (2007) p62/SQSTM1 binds directly to Atg8/LC3 to facilitate degradation of ubiquitinated protein aggregates by autophagy. J Biol Chem 282:24131–24145. CrossRef Medline

Sathasivam K, Lane A, Legleiter J, Warley A, Woodman B, Finkbeiner S, Paganetti P, Muchowski PJ, Wilson S, Bates GP (2010) Identical oligomeric and fibrillar structures captured from the brains of R6/2 and knock-in mouse models of Huntington's disease. Hum Mol Genet 19:65–78. CrossRef Medline

Saudou F, Finkbeiner S, Devys D, Greenberg ME (1998) Huntingtin acts in the nucleus to induce apoptosis but death does not correlate with the formation of intranuclear inclusions. Cell 95:55–66. CrossRef Medline

Sobue G, Hashizume Y, Mukai E, Hirayama M, Mitsuma T, Takahashi A (1989) X-linked recessive bulbospinal neuronopathy. A clinicopathological study. Brain 112:209–232. CrossRef Medline

Tokui K, Adachi H, Waza M, Katsuno M, Minamiyama M, Doi H, Tanaka K, Hamazaki J, Murata S, Tanaka F, Sobue G (2009) 17-DMAG ameliorates polyglutamine-mediated motor neuron degeneration through well-preserved proteasome function in an SBMA model mouse. Hum Mol Genet 18:898–910. CrossRef Medline

Troakes C, Maekawa S, Wijesekera L, Rogelj B, Siklós L, Bell C, Smith B, Newhouse S, Vance C, Johnson L, Hortobágyi T, Shatunov A, Al-Chalabi A, Leigh N, Shaw CE, King A, Al-Sarraj S (2012) An MND/ALS phenotype associated with C9orf72 repeat expansion: abundant p62-positive, TDP-43-negative inclusions in cerebral cortex, hippocampus and cerebellum but without associated cognitive decline. Neuropathology 32:505–514. CrossRef Medline

Walcott JL, Merry DE (2002) Ligand promotes intranuclear inclusions in a novel cell model of spinal and bulbar muscular atrophy. J Biol Chem 277:50855–50859. CrossRef Medline

Watase K, Weeber EJ, Xu B, Antalffy B, Yuva-Paylor L, Hashimoto K, Kano M, Atkinson R, Sun Y, Armstrong DL, Sweatt JD, Orr HT, Paylor R, Zoghbi HY (2002) A long CAG repeat in the mouse Sca1 locus replicates SCA1 features and reveals the impact of protein solubility on selective neurodegeneration. Neuron 34:905–919. CrossRef Medline

Waza M, Adachi H, Katsuno M, Minamiyama M, Sang C, Tanaka F, Inukai A, Doyu M, Sobue G (2005) 17-AAG, an Hsp90 inhibitor, ameliorates polyglutamine-mediated motor neuron degeneration. Nat Med 11:1088–1095. CrossRef Medline

Yoo SY, Pennesi ME, Weeber EJ, Xu B, Atkinson R, Chen S, Armstrong DL, Wu SM, Sweatt JD, Zoghbi HY (2003) SCA7 knockin mice model human SCA7 and reveal gradual accumulation of mutant ataxin-7 in neurons and abnormalities in short-term plasticity. Neuron 37:383–401. CrossRef Medline

PLOS ONE

dnc-1/dynactin 1 Knockdown Disrupts Transport of Autophagosomes and Induces Motor Neuron Degeneration

Kensuke Ikenaka[1], Kaori Kawai[1], Masahisa Katsuno[1], Zhe Huang[1], Yue-Mei Jiang[1], Yohei Iguchi[1], Kyogo Kobayashi[2], Tsubasa Kimata[2], Masahiro Waza[1], Fumiaki Tanaka[1], Ikue Mori[2], Gen Sobue[1,3]*

1 Department of Neurology, Nagoya University Graduate School of Medicine, Nagoya, Japan, **2** Group of Molecular Neurobiology, Nagoya University Graduate School of Science, Nagoya, Japan, **3** Core Research for Evolutional Science and Technology (CREST), Japan Science and Technology Agency (JST), Saitama, Japan

Abstract

Amyotrophic lateral sclerosis (ALS) is a fatal neurodegenerative disease characterized by the progressive loss of motor neurons. We previously showed that the expression of dynactin 1, an axon motor protein regulating retrograde transport, is markedly reduced in spinal motor neurons of sporadic ALS patients, although the mechanisms by which decreased dynactin 1 levels cause neurodegeneration have yet to be elucidated. The accumulation of autophagosomes in degenerated motor neurons is another key pathological feature of sporadic ALS. Since autophagosomes are cargo of dynein/dynactin complexes and play a crucial role in the turnover of several organelles and proteins, we hypothesized that the quantitative loss of dynactin 1 disrupts the transport of autophagosomes and induces the degeneration of motor neuron. In the present study, we generated a *Caenorhabditis elegans* model in which the expression of DNC-1, the homolog of dynactin 1, is specifically knocked down in motor neurons. This model exhibited severe motor defects together with axonal and neuronal degeneration. We also observed impaired movement and increased number of autophagosomes in the degenerated neurons. Furthermore, the combination of rapamycin, an activator of autophagy, and trichostatin which facilitates axonal transport dramatically ameliorated the motor phenotype and axonal degeneration of this model. Thus, our results suggest that decreased expression of dynactin 1 induces motor neuron degeneration and that the transport of autophagosomes is a novel and substantial therapeutic target for motor neuron degeneration.

Citation: Ikenaka K, Kawai K, Katsuno M, Huang Z, Jiang Y-M, et al. (2013) *dnc-1/dynactin 1* Knockdown Disrupts Transport of Autophagosomes and Induces Motor Neuron Degeneration. PLoS ONE 8(2): e54511. doi:10.1371/journal.pone.0054511

Editor: Udai Pandey, Lousiana State University Health Sciences Center, United States of America

Received October 2, 2012; **Accepted** December 12, 2012; **Published** February 7, 2013

Funding: This work was supported by Grants-in-Aid for Scientific Research and Global COE Program from the Ministry of Education, Culture, Sports, Science, and Technology, Grants-in-Aid for Scientific Research from the Ministry of Health, Labor, and Welfare, a Grant-in-Aid for Scientific Research on Innovated Areas "Foundation of Synapse and Neurocircuit Pathology", and Core Research for Evolutional Science and Technology (CREST) from Japan Science and Technology Agency (JST). The funders had no role in study design, data collection and analysis, decision to publish, or preparation of the manuscript.

Competing Interests: The authors have declared that no competing interests exist.

* E-mail: sobueg@med.nagoya-u.ac.jp

Introduction

Autophagy is one of the major cellular systems that regulate protein degradation and organelle turnover in physiological and pathological conditions [1], and it is an essential quality control system for proteins in post-mitotic neurons that need to eliminate abnormal proteins and organelles for their proper function and survival [2,3]. It is well known that the dysregulation of autophagy causes neurodegeneration [4,5] and that the abnormal accumulation of autophagosomes is observed in several neurodegenerative diseases [6–9]. Particularly, intensified immunoreactivity for microtubule-associated protein 1 light chain 3 (LC3), which is a marker of autophagosome, is often observed in the spinal motor neurons of amyotrophic lateral sclerosis (ALS) patients [8,10]. Electron microscopy of the motor neurons of ALS patients shows an increased number of autophagosomes surrounded by a double-membrane that contain sequestered cytoplasmic organelles, e.g., mitochondria [8]. Although these observations suggest the possibility that autophagy is upregulated to protect neurons from increased amounts of aggregated proteins and/or damaged organelles, it is also possible that the accumulation of autophagosomes due to dysregulated autophagy leads to neurodegeneration.

One possible mechanism for the accumulation of autophagosomes in degenerated neurons is the disruption of the cellular transport system, given that autophagosomes are cargo that moves bidirectionally along microtubules, which is powered by the kinesin family of motor proteins and dynein/dynactin complexes [11,12]. We previously investigated the motor neuron-specific gene expression profile of sporadic ALS (SALS), which accounts for more than 90% of ALS, and found that the expression of dynactin 1, which is a key member of the dynactin family, is markedly decreased in the spinal motor neurons of SALS patients [9]. The decreased expression of dynactin 1 was also verified quantitatively using *in situ* hybridization analysis of tissues from SALS patients [13]. By contrast, the expression of other motor proteins including the kinesin family, which are responsible for anterograde transport and dyneins, which are responsible for retrograde transport was not significantly changed. Thus, we hypothesized that the decreased expression of dynactin 1 results in the disrupted transport of autophagosomes and thus attenuates the protective effects of autophagy against neurodegeneration.

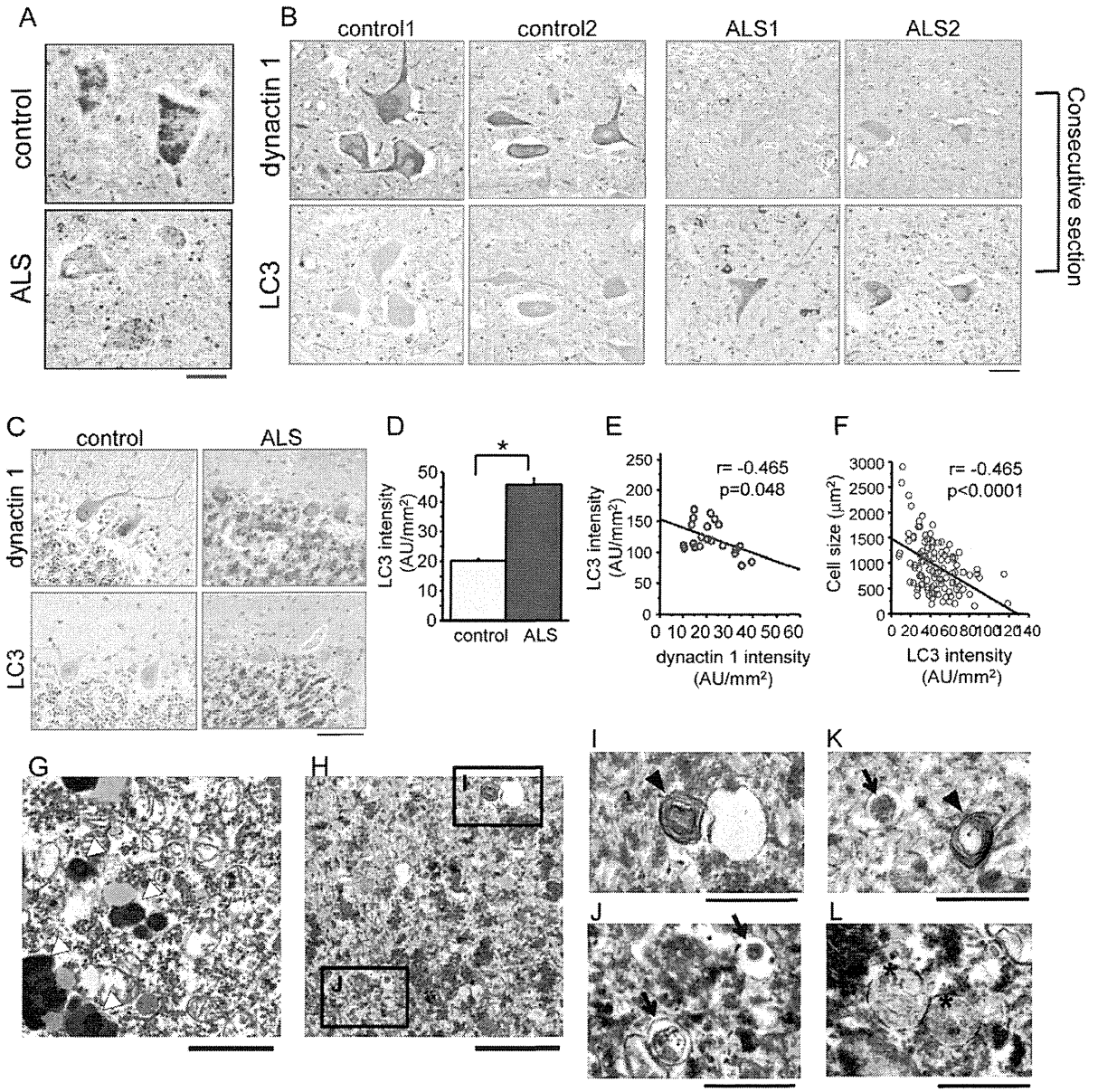

Figure 1. Dysregulated expression of dynactin 1 and the accumulation of autophagosomes in SALS patients. (*A*) Representative *in situ* hybridization for *DCTN1* in the spinal cords of control and ALS patients. (*B, C*) Representative immunohistochemistry for dynactin 1 and microtubule-associated protein 1 light chain 3 alpha (LC3) on consecutive spinal cord (*B*) and cerebellar (*C*) sections from control and ALS patients. (*D*) Quantification of the signal intensity of LC3 in anterior horn neurons of the spinal cord (n = 20 sections from 4 patients for each group). (*E*) Correlation between LC3 intensity and the expression of *DCTN1* in individual motor neurons from SALS patients (n = 12 consecutive sections from 3 SALS patients). (*F*) Correlation between the intensity of LC3 immunoreactivity and the size of motor neurons in SALS patients (n = 20 sections from 4 patients). (*G–L*) Electron microscopy images of spinal motor neurons. Representative lower magnification image of a motor neuron from a control patient (*G*) and lower (*H*) and higher magnification images (*I–L*) from SALS patients. The open arrowheads indicate lipofuscin. There were abundant autophagic vacuoles, e.g., multi-lamellar bodies (arrowheads in *I, K*), autophagosome-like double membrane vesicles (arrows in *K, J*), and autolysosomes (asterisks in *L*) in the motor neurons of SALS patients, but not of the control. Scale bar = 50 μm (*A–C*), 2 μm (*G, H*), or 1μm (*I–L*). Statistical analyses were performed using Student's t test (*p<0.0001) and Pearson's correlation coefficient in *E* and *F*. The error bars are S.E.M.
doi:10.1371/journal.pone.0054511.g001

Moreover, mutations of *DCTN1*, the gene encoding dynactin 1, are linked to familial lower motor neuron disease [14]. Several mutant *DCTN1* models exhibited motor dysfunction and pathological changes related to motor neuron disease [15,16]. As seen in the motor neurons of SALS patients, mutant *DCTN1* mice exhibited a massive accumulation of membrane vesicles, including autophagosomes, in spinal motor neurons [16]. Although these findings suggest that impaired vesicular trafficking might cause the accumulation of vesicles, it remains unclear whether the transport of autophagosomes is actually impaired in the mutant *DCTN1* mice or whether the accumulation of autophagosomes plays a causative role in the pathogenesis of motor neuron degeneration.

The aim of the present study was to clarify the biological link between the quantitative loss of dynactin 1 and the disruption of autophagy. In particular, we examined whether the decreased levels of dynactin 1 induce motor neuron degeneration by

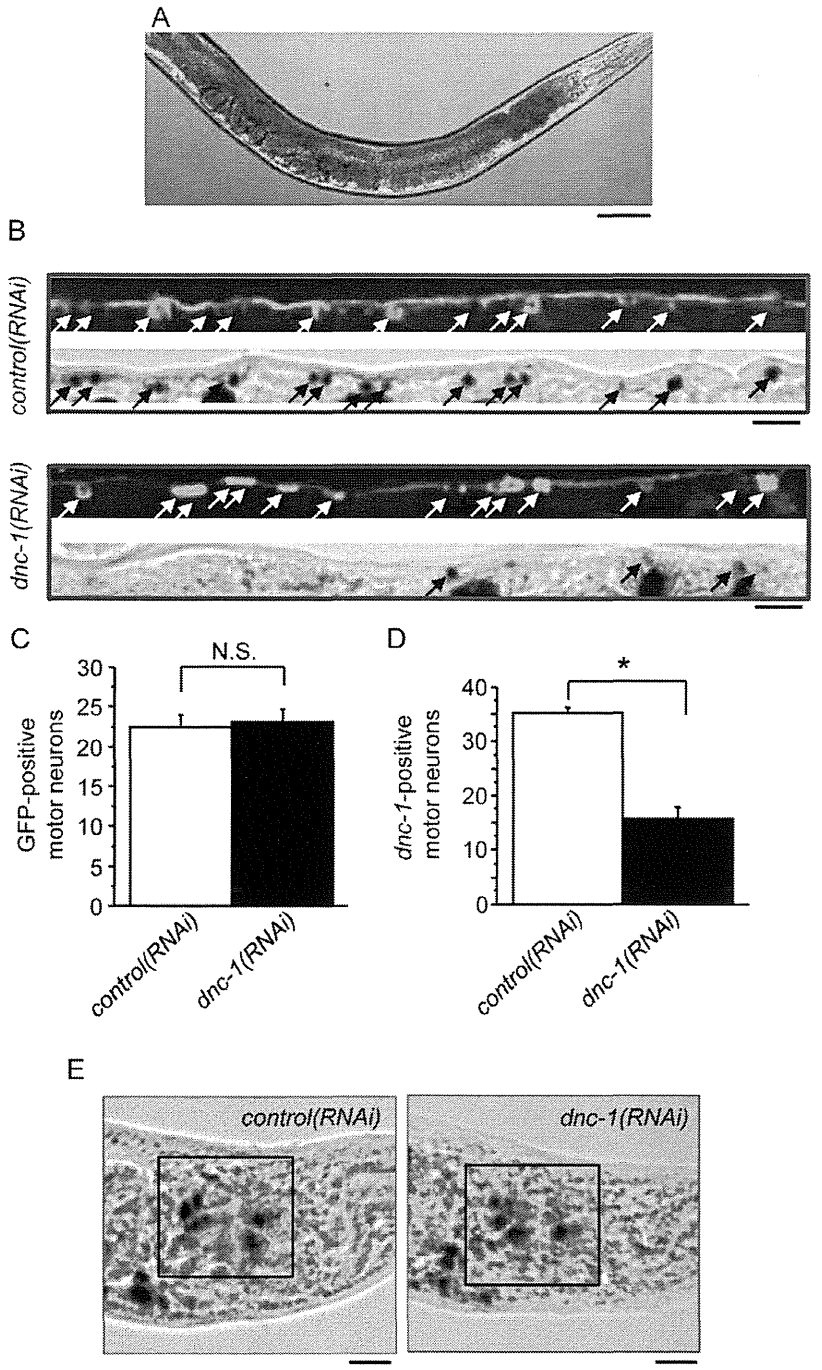

Figure 2. Creation of the motor neuron-specific *dnc-1*-KD *C. elegans* model. (*A*) Fluorescent visualization of ventral cholinergic motor neurons and their neurites in transgenic *C. elegans* worms expressing acr2p::*shRNA*::*gfp*. (*B*) Representative immunohistochemical staining of GFP and *in situ* hybridization against *dnc-1* in ventral cholinergic motor neurons and their neurites in the *control(RNAi)* and *dnc-1(RNAi)* worms. (*C*) The number of GFP-positive motor neurons (white arrows in *B*) was not significantly different between the *control(RNAi)* and *dnc-1(RNAi)* worms (n = 20 animals for each strain). (*D*) Conversely, the number of *dnc-1* mRNA-positive neurons (black arrows in *B*) was remarkably decreased in the *dnc-1(RNAi)* worms (n = 20 animals for each strain). (*E*) Representative images of *in situ* hybridization for *dnc-1* in the head neurons. Scale bars = 100 μm (*A*), 10 μm (*B*), and 20 μm (*E*). Statistical analyses were performed using Student's t test (*$p<0.0001$). The error bars are S.E.M.
doi:10.1371/journal.pone.0054511.g002

hindering the transport of autophagosomes. To this end, we first examined the relationship between the decreased levels of dynactin 1, the accumulation of autophagosomes, and motor neuron degeneration in post-mortem tissues from SALS patients. Next, we created a *Caenorhabditis elegans (C. elegans)* model of the motor neuron-specific knockdown (KD) of *dnc-1*, the *C. elegans* homolog of human *DCTN1*, using small hairpin RNA (shRNA), and investigated whether the depletion of dynactin 1 impairs the transport of autophagosomes and thereby induces motor neuron degeneration. Using this model, we also explored therapeutic strategies targeting the transport of autophagosomes.

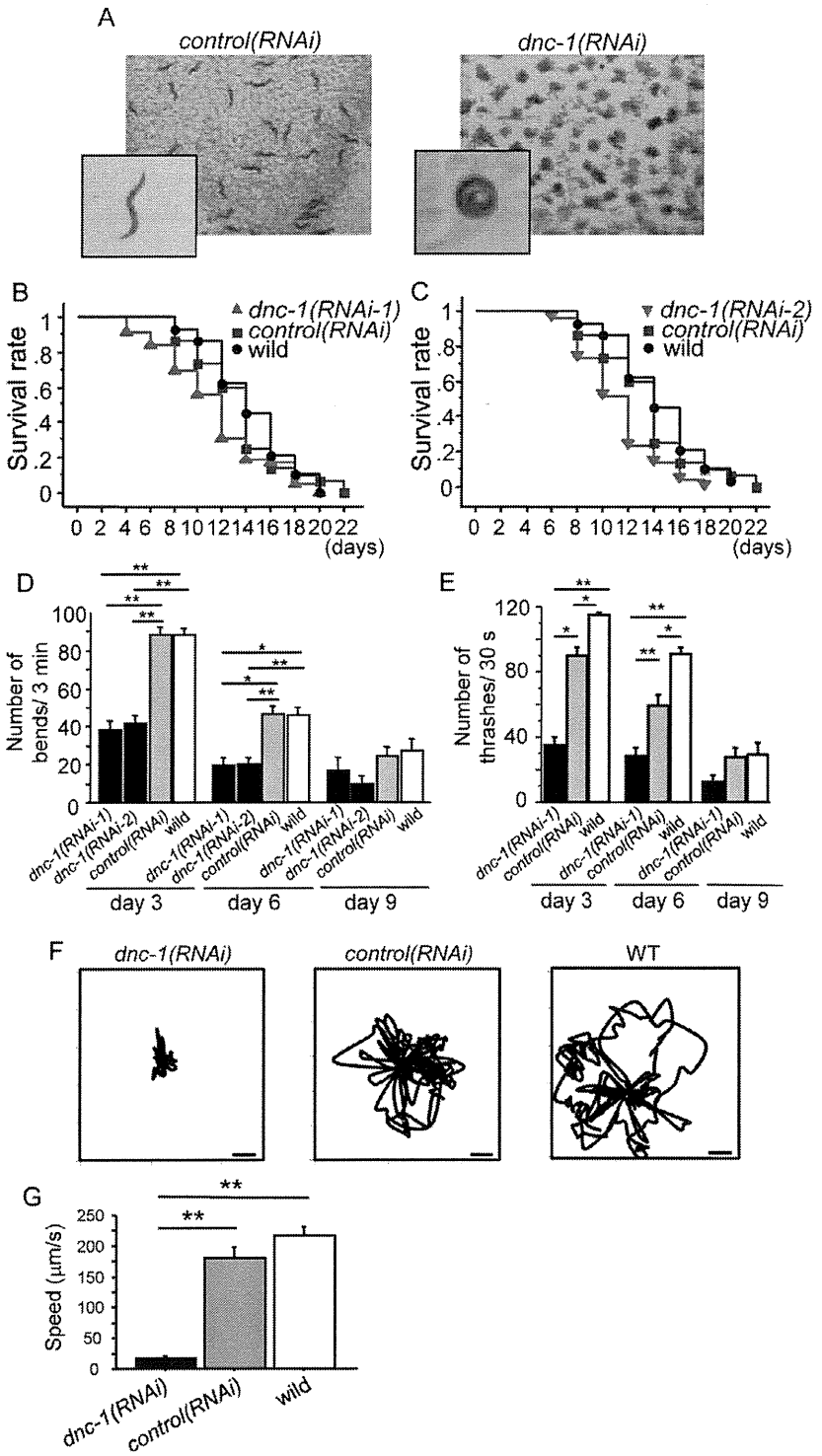

Figure 3. Motor dysfunction in the motor neuron-specific *dnc-1*-KD *C. elegans* model. (*A*) Stereoscopic microscopy showing the phenotypes of the *control(RNAi)* and *dnc-1(RNAi)* worms. (*B, C*) Survival curves of the transgenic worms (*dnc-1(RNAi-1)*, n = 90; *dnc-1(RNAi-2)*, n = 90; *control(RNAi)* n = 90; and wild-type n = 30). The same survival data of the *control(RNAi)*and wild-type worms were used in both graphs. Both *dnc-1(RNAi)* worms with different shRNA sequences (101, 2888) had significantly reduced life spans compared with the *control(RNAi)* worms (101: p = 0.005; 2888: p<0.0001; log-rank test). (*D*) The number of body bends associated with forward movement in 3 min. (*E*) The number of thrashing movements in liquid medium in 30 s. (*F, G*) The tracks (*F*) and average speed of the worms (*G*) analyzed by video capture at day 4. Scale bars in *F* = 100 μm. The error bars are S.E.M. (n = 30, 30, 40, and 40 for *dnc-1(RNAi-1)*, *dnc-1(RNAi-2)*, *control(RNAi)*, and wild-type, respectively, in *D*, *E*; and n = 6, 6, and 6 for *dnc-1(RNAi-1)*, *control(RNAi)*, and wild-type, respectively, in *G*). The statistical analyses in *C*, *D*, and *F* were performed by one-way ANOVA followed by the Bonferroni/Dunn post hoc test (*p<0.001 and **p<0.0001).
doi:10.1371/journal.pone.0054511.g003

Materials and Methods

Protocols for the human samples

Ethics Statement. The collection of autopsied human tissues and their use for this study were approved by the Ethics Committee of Nagoya University Graduate School of Medicine, and written informed consent was obtained from the patients' next-of-kin. Experimental procedures involving human subjects were conducted in conformance with the principles expressed in the Declaration of Helsinki.

Immunohistochemistry. Six micrometer-thick sections from paraffin-embedded spinal cord sections from autopsied patients were prepared as described previously [17]: four patients with sporadic ALS (64.5±9.3 years-old; M:F = 2:2) and four disease controls (73.5±5.4 years-old; M:F = 1:3). The four control patients were diagnosed with progressive supranuclear palsy, multiple system atrophy, diffuse lewy body disease, and Parkinon's disease, respectively. The sections were first microwaved for 20 min in 50 mM citrate buffer, pH 6.0, then blocked with TNB blocking buffer (PerkinElmer, Hvidovre, Denmark) in Tris-

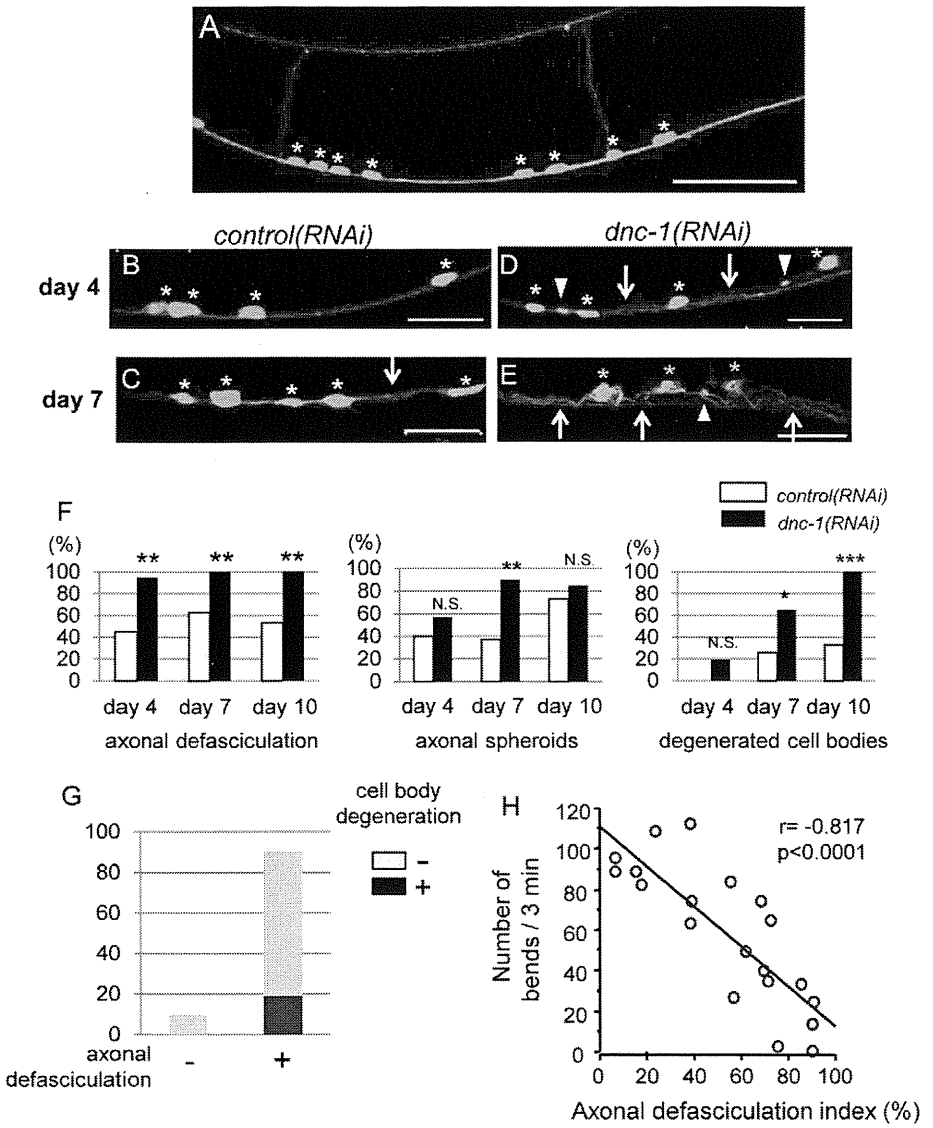

Figure 4. Morphological changes in ventral motor neurons. (*A*) Representative view of fluorescent GFP microscopic images of the ventral nerve cord in a *control(RNAi) C. elegans*. All of the motor neurons (white asterisks) were located in the ventral side of the worm. Axons from the motor neurons project within the ventral nerve cord or toward the dorsal side. (*B–E*) Representative view of the ventral nerve cord in the *control(RNAi)* worms (*B, C*) and *dnc-1(RNAi)* worms (*D, E*). The degenerated axons were defasciculated (arrows in *D, E*) and formed spheroids (arrowheads in *D, E*) in the *dnc-1(RNAi)* worms. Mild defasciculation was observed occasionally in the *control(RNAi)* worms (arrow in *C*). While the cell bodies of the motor neurons were regular and round in *control(RNAi)* and young adult *dnc-1(RNAi)* worms (white asterisks in *B–D*), abnormally shaped cell bodies (yellow asterisks in *E*) were observed only in the worms with severe axonal changes. (*F*) Semi-quantification of the abnormal morphological changes in the *control(RNAi)* and *dnc-1(RNAi)* worms. The percentage of worms with axonal defasciculation, axonal spheroids, or cell body degeneration on days 4, 7, and 10. (*G*) Population of *dnc-1(RNAi)* worms with and without cell body degeneration (black and gray boxes, respectively) on day 4. (*H*) Correlation between the axonal defasciculation index and locomotor function in the *dnc-1(RNAi)* worms. The axonal defasciculation index represents the degree of axonal defasciculation (its details are described in the Materials and Methods). Scale bars = 20 μm. The statistical analysis in *F* was performed using Fisher's exact probability test (*p<0.05, **p<0.001, and ***p<0.0001) and Pearson's correlation coefficient in *H*.
doi:10.1371/journal.pone.0054511.g004

buffered saline (pH 7.5) at room temperature for 30 min and incubated with a monoclonal antibody against LC3 (anti-LC3, 1:40000; Medical & Biological Laboratories, Co., Nagoya, Japan) or dynactin 1 (anti-dynactin 1 H300; 1:2000; Santa Cruz, Santa Cruz, CA, USA) overnight at 4°C. The subsequent procedures were carried out using the EnVision+Kit/HRP (DAB) (DAKO, Glostrup, Denmark) according to the manufacturer's protocol.

Quantitative assessment of immunohistochemistry. To assess LC3 immunoreactivity in spinal motor neurons, we included 4 ALS patients and 4 disease controls, and prepared 5 independent specimens from each subject. We counted about 200 motor neurons in ALS patients and about 400 neurons in control patients. The intensity of immunohistochemistry signals was quantified using a BZ-8000 fluorescent microscope and its software (BZ-Analyzer; Keyence, Osaka, Japan). Signal intensity was expressed as the individual intracellular cytoplasmic signal level (arbitrary absorbance units/mm^2) per motor neuron by subtracting the mean background levels of 3 regions of interest in each section. The ventral spinal horn was defined as the gray matter ventral to the line through the central spinal canal perpendicular to the ventral spinal sulcus. To investigate the correlation between dynactin 1 and LC3 in individual motor neurons we used consecutive transverse spinal cord sections.

***In situ* hybridization.** *In situ* hybridization for human tissue was performed as described previously [13]. We provide the detailed information in Materials and Methods S1.

Electron microscopy. Electron microscopy was performed on samples from 2 sporadic ALS patients (71 years-old male and 62 years-old female) and 2 disease control patients (68 years old male with multiple system atrophy and 60 years-old male with multiple system atrophy). Epoxy resin-embedded specimens of spinal anterior horn were cut into 70-nm ultrathin sections. Ultrathin sections were contrasted by staining with uranyl acetate and lead citrate. Sections were viewed with a JEM-1400EX electron microscope (JEOL, Tokyo, Japan) at 80 kV.

Protocols for *C. elegans*

Ethics statement. All animal experiments were performed in accordance with the National Institute of Health Guide for the Care and Use of Laboratory Animals and were approved by the Nagoya University Animal Experiment Committee.

Culture of *C. elegans*. Standard methods were used to culture *C. elegans* on nematode growth medium (NGM) agar [18]. The animals were maintained at 20°C unless otherwise indicated. We provide the detailed information in Materials and Methods S1.

Constructs and *C. elegans* Strains. To generate transgenic *C. elegans*, plasmid DNA encoding acr2promotor::*shRNA*::*gfp* was injected into the gonads of young adult hermaphrodite N2 worms. We provide the detailed information for the shRNA vector and other co-injected proteins, i.e., SNB-1 and Lgg1, in Materials and Methods S1.

Whole Mount *in situ* Hybridization. Whole mount *in situ* hybridization of worms was performed as described previously [13,19]. We provide the detailed information in Materials and Methods S1.

Phenotypic analysis of *C. elegans*. A lifespan assay was performed as described preciously [20], with some modifications. The Worms were allowed to lay eggs on a dish for 3–6 h to obtain synchronous progeny for the experiment. L4 worms were collected and transferred every 3 days to a fresh plate until the end of their reproductive life. The animals were scored as dead if they did not move when prodded with a platinum pick and did not show pharyngeal pumping.

A body bend assay, liquid thrashing assay, and video capture analysis were performed as locomotion assays. To examine the body bend frequency, exposed worms were transferred onto a fresh NGM plate and scored for the number of body bends

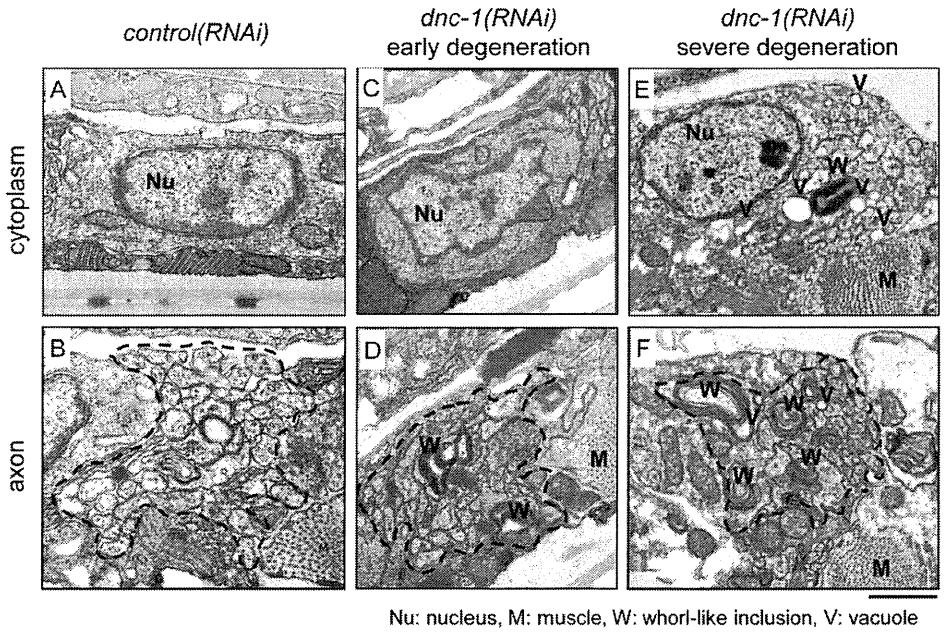

Figure 5. Ultrastructure of degenerating motor neurons. Electron microscopy of transverse sections of ventral motor neurons from the *control(RNAi)* (*A, B*) and *dnc-1(RNAi)* (*C–F*) worms. The dashed lines in *B*, *D*, and *F* denote the boundaries of the main bundle of axons. Each round-shaped component inside the dashed line is an axon. In the *dnc-1(RNAi)* worms, whorl-like inclusions (W) and vacuoles (V) were observed (*D–F*). In the worms with mild axonal degeneration (*D*), few morphological changes were observed in the cytoplasm (*C*); however, in the later stage with severe axonal degeneration (*F*), the cell bodies were also affected (*E*). Scale bars = 20 μm.
doi:10.1371/journal.pone.0054511.g005

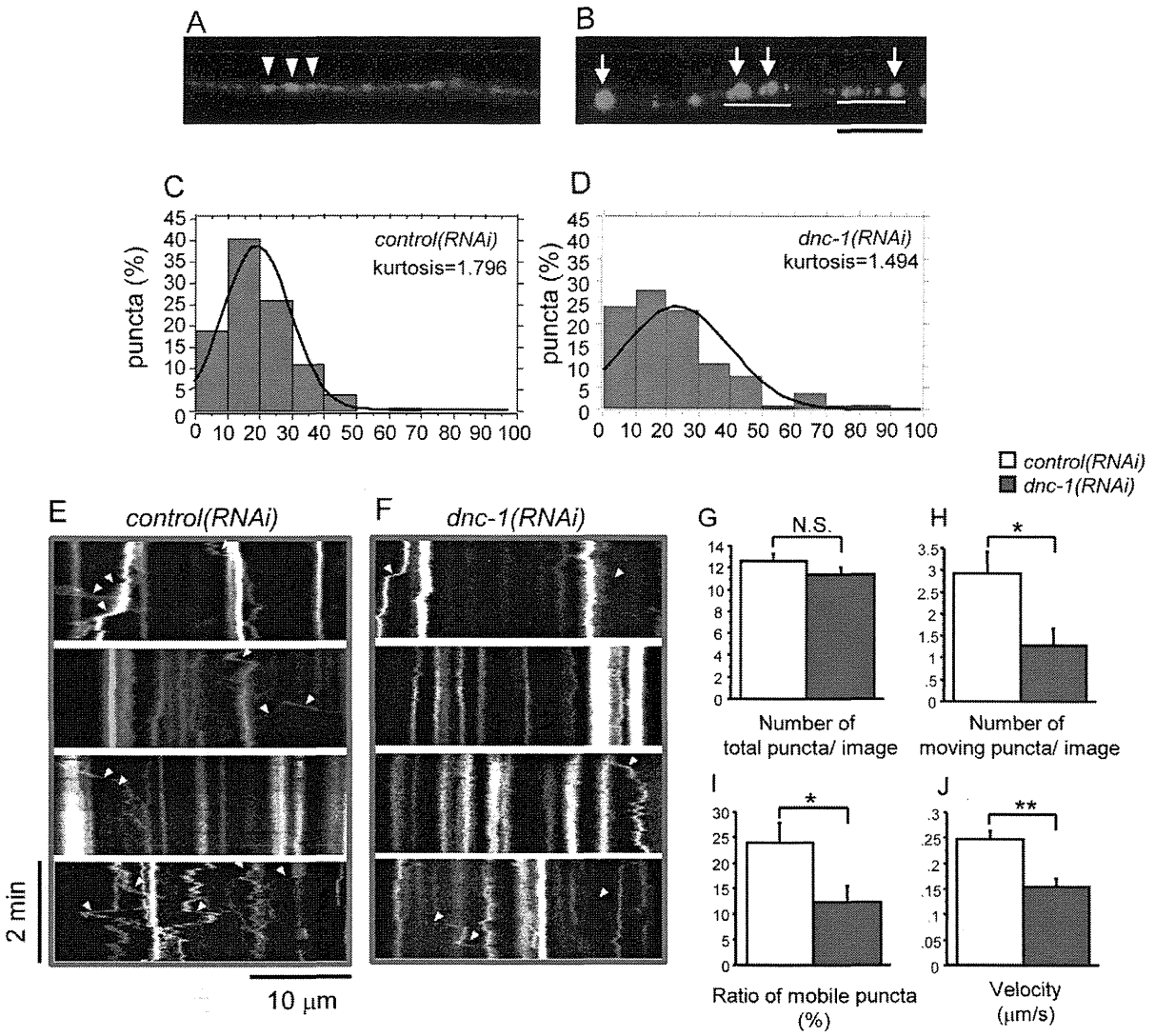

Figure 6. Defective axonal transport of synaptobrevin-1 in *dnc-1(RNAi) C. elegans.* (*A, B*) Expression patterns of DsRed-tagged synaptobrevin-1 (SNB-1) in the dorsal nerve cord. In the *control(RNAi)* worms, SNB-1 puncta (arrowheads) are regularly spaced with a uniform shape. In the *dnc-1(RNAi)* worms (B), they are irregularly spaced and abnormally accumulated (white bars) with occasional clumps. (*C, D*) Histograms of the distances between neighboring SNB-1 puncta. The average distance between puncta in the *control(RNAi)* (3.240±1.716 μm, n = 139) and *dnc-1(RNAi)* (3.855±2.764 μm, n = 104) worms was not significantly different (p = 0.996 by Student's t test), but the peak of the control histogram was higher than that of the *dnc-1(RNAi)* histogram, proving that the localization of SNB1 was irregular. (*E, F*) Representative kymographs of SNB-1::DsRed in the ventral nerve cord from the *control(RNAi)* (*E*) and *dnc-1(RNAi)* (*F*) worms derived from time-lapse imaging. Vertical lines represent stationary/docked SNB-1 puncta and oblique lines (labeled with yellow arrowheads) represent the tracks of moving SNB-1 puncta. The slope of this track is an indicator of velocity. (*G*) The number of SNB-1 puncta within a single image of kymograph was not different between the *control(RNAi)* and the *dnc-1(RNAi)* worms. (*H*) The mean velocities of SNB-1 puncta. (*I, J*) The quantitative analysis of mobile puncta. The number of puncta which moved more than 2 μm was counted (*I*). The ratio of moving puncta was calculated by dividing the number of moving puncta by the total number of SNB-1 puncta (*J*). A total of 20 time laps images were analyzed from each strains in *G–J*. Scale bar (black) = 10 μm (*B*). Statistical analyses were performed using Student's t test (*p<0.05, **p<0.001, ***p<0.0001). Error bars are S.E.M.
doi:10.1371/journal.pone.0054511.g006

performed in 3 min. A body bend was defined as a change in the direction of the part of the worm corresponding to the posterior bulb of the pharynx along the y-axis, assuming that the worm was traveling along the x-axis. We also performed a liquid thrashing assay as described previously [21], with some modifications. Briefly, the worms were put on a 6-cm NGM-coated plate with 3 ml of M9 media. The worms were allowed to settle for 30 s, their movements were captured by video for 30 s, and the number of thrashing movements was counted. We also analyzed the speed of movement using a video capture system as described previously [22]. Briefly, fully matured, adult worms were transferred individually to agar plates with no food. The movement of each worm was observed for 5 min and recorded using video equipment (Olympus, Tokyo, Japan) with a sampling rate of 30 frames/s. A computer-controlled microscope stage was automatically moved to center the worms in the visual field using a custom image analysis algorithm within the microscope's software package (MetaMorph; Universal Imaging Corp., West Chester, PA, USA). The midlines of the recorded worms were extracted from each image. All strains were randomized and scored on the same day.

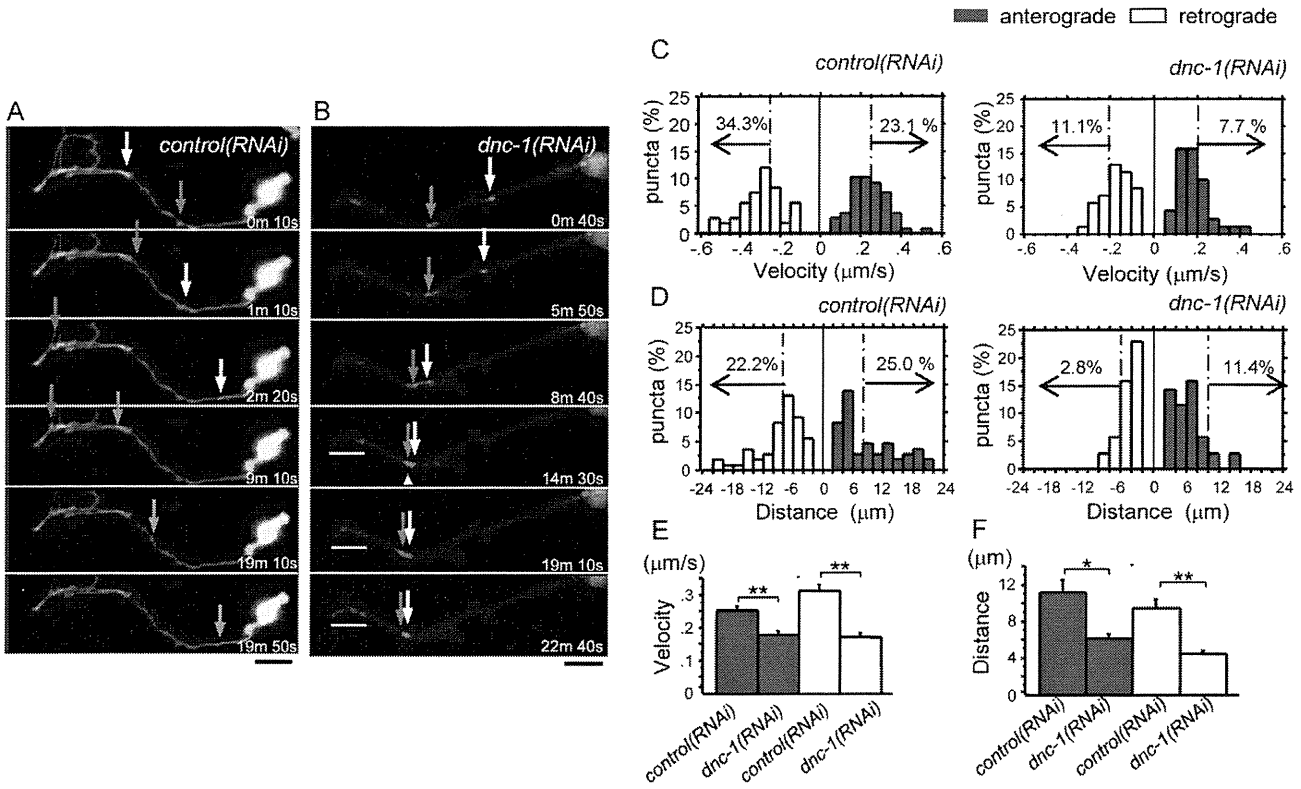

Figure 7. Impaired transport and abnormal accumulation of autophagosomes in the axons of *dnc-1(RNAi)* motor neurons. (*A, B*) Representative time-lapse images of autophagosome (DsRed-tagged Lgg1) transport in an axon (GFP-tagged shRNA; green) of a primary cultured motor neuron from the *control(RNAi)* (*A*) and *dnc-1(RNAi)* (*B*) worms. The autophagosomes were transported smoothly along the axon (arrows) of the *control(RNAi)* motor neuron (*A*). The autophagosome (arrows) was transported anterogradely, but was trapped where the axon was slightly narrowed (arrowhead) (*B*). There were also autophagosomes that accumulated in the distal part of the axon (*B*, bar). (*C*) Histograms of Lgg1::DsRed velocity in the retrograde (white bars) and anterograde (black bars) directions in neurons from the *control(RNAi)* and *dnc-1(RNAi)* worms. (*D*) Histograms of Lgg1::DsRed run-length in the *control(RNAi)* and *dnc-1(RNAi)* neurons. (*E, F*) Mean velocity (*E*) and run-length (*F*) of autophagosomes (n = 70 vesicles for each strain) in *control(RNAi)* and *dnc-1(RNAi)* neurons. Scale bar = 5 μm (A and B). The statistical analyses in *E* and *F* were performed using the Mann-Whitney U test (*$p<0.05$ and **$p<0.0001$). The error bars are S.E.M.
doi:10.1371/journal.pone.0054511.g007

Preparation of starved worms for the dietary restriction assay. All worms were synchronized by egg preparation [23]. The eggs were incubated at 20°C for 48 h in liquid medium. After 48 h, newly hatched worms were washed 3 times with distilled water, transferred to S basal medium without OP50, and incubated for 24 h. Worms were then picked randomly and used for the liquid thrashing assay.

Drug treatment. The worms were synchronized by egg preparation and incubated at 20°C for 24 h in liquid medium. They were then treated with rapamycin (LC Laboratories, Woburn, MA, USA) dissolved in ethanol at a final concentration of 10 or 100 μM, 3-methyladenine (3-MA) (SIGMA) dissolved in DMSO at a final concentration of 1 or 10 mM, or trichostatin A (TSA) (Tokyo Chemical Industry, Co., Tokyo, Japan) dissolved in DMSO at a final concentration of 1, 10, or 100 μM and incubated in liquid medium for 48 h. For controls (0 μM), ethanol or DMSO was added. Worms were then picked randomly and used for the liquid thrashing assay or microscopic analysis.

Primary neuronal cell cultures of nematodes. Primary neuronal cell cultures were prepared as described previously [24], with some modifications. In the present study, in order to obtain larger number of gravid animals, we cultured the worms in liquid medium (S basal medium with concentrated OP50) as described previously [25]. After incubation in liquid medium for 3 days, we performed egg isolation using lysis buffer (0.5 M NaOH/1% NaClO). Then we removed eggshell by enzymatic digestion using chitinase (SIGMA) and isolated embryonic cells were plated onto peanut lectin-coated glass bottom dishes (IWAKI, Tokyo, Japan).

Microscopic analysis. The worms were anesthetized by placing them in an 8-μl drop of levamisole (2 mM) on solidified pads of 2% agarose laid on slides. After coverslipping, the worms were examined under an LSM710 confocal microscope (Carl Zeiss Inc., Thornwood, NJ, USA). The regularity of SNB-1::DsRed localization/spacing was evaluated by measuring the distance between two neighboring fluorescent puncta of SNB-1::DsRed using ImageJ 1.43 software (National Institutes of Health). The axonal defasciculation index was measured as follows. The ventral nerve cord was divided into compartments consisting of two neighboring motor neurons. We counted the number of compartments with axonal defasciculation and divided it by the total number of compartments.

In vivo analysis of autophagosome mobility was performed as follows. Lgg1::DsRed worms were plated on an agar pad and observed using confocal microscopy. The red puncta, which represent autophagosomes, were observed for 1 min. The number of autophagosomes that moved within 1 min was divided by the total number of autophagosomes observed.

***In vitro* transport assay and image analysis.** Time-lapse images were acquired at room temperature using a 63× oil-immersion objective (N.A 1.4) for live-cultured neuron analysis at

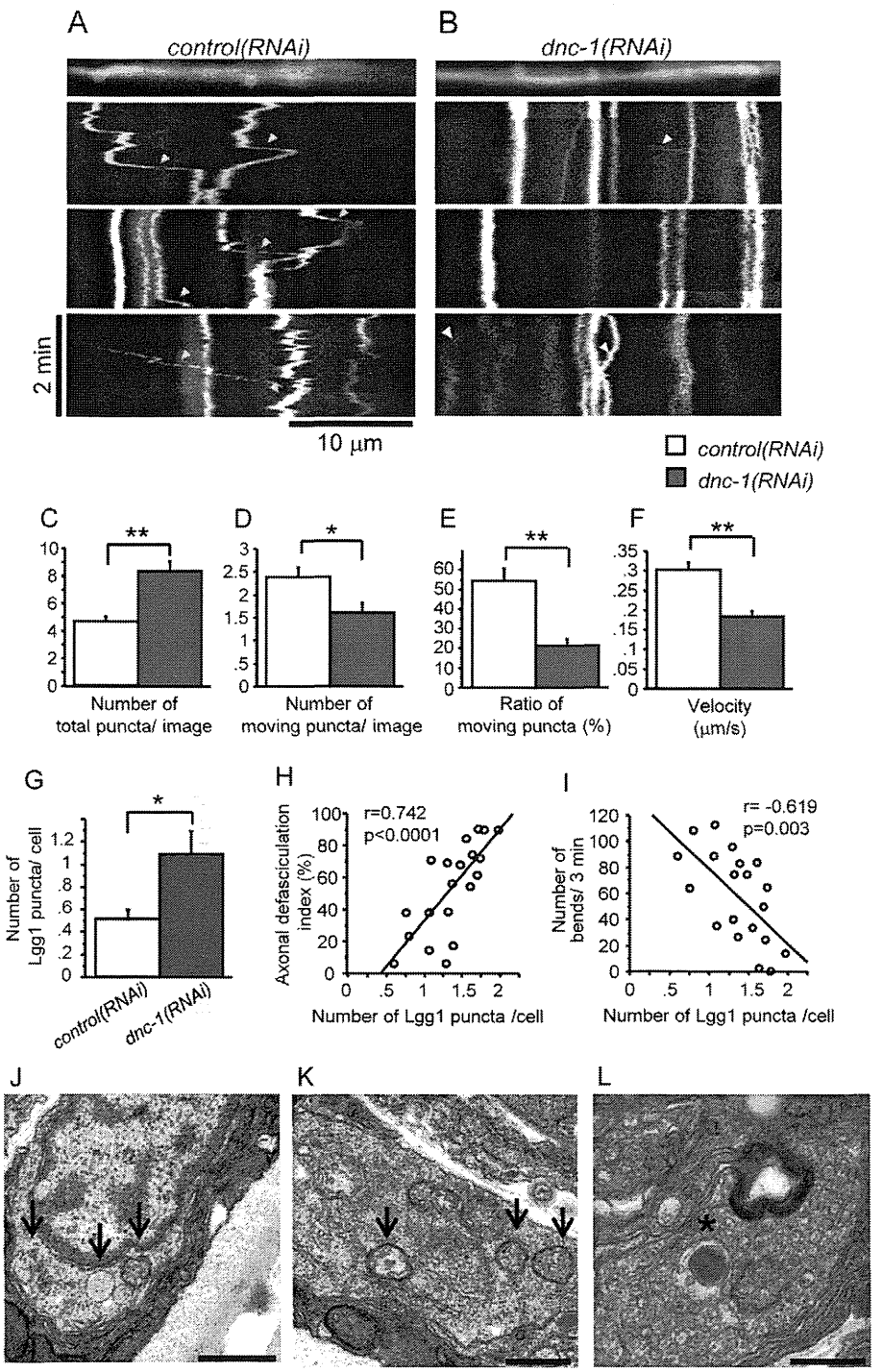

Figure 8. Accumulation of autophagosomes and motor neuron degeneration in the *dnc-1(RNAi)* worms. (*A, B*) Representative kymographs of Lgg1::DsRed in the ventral nerve cord from the *control(RNAi* (*A*) and *dnc-1(RNAi)* (*B*) worms derived from time-lapse images. Vertical lines represent stationary/docked Lgg1 puncta, while the oblique lines (labeled with arrowheads) represent the tracks of moving Lgg1 puncta. The slope of this track is an indicator of velocity. (*C*) The number of Lgg1 puncta within a single kymograph image. (*D, E*) Quantitative analyses of the mobility of puncta. The number of puncta that moved more than 2 μm was counted (*D*). The ratio of moving puncta was calculated by dividing the number of moving puncta by the total number of puncta (*E*). (*F*) The mean velocities of Lgg1 puncta. A total of 20 time-lapse images were analyzed for each strain in *C–F*. (*G*) The number of Lgg1 puncta was increased in the *dnc-1(RNAi)* worms compared with the *control(RNAi)* worms (n = 15 for each group). (*H, I*) Accumulation of autophagosomes in the *dnc-1(RNAi)* worms was correlated with the severity of axonal defasciculation (*H*) and locomotor function (*I*) (n = 20 for each analysis). (*J–L*) Ultrastructural images of ventral motor neurons from the *dnc-1(RNAi)* worms. Aberrant membranous vesicles including degenerated mitochondria were observed in the cytoplasm (*J*) and axons (*K*) (arrows). Autophagosome-like, double membrane vesicles (asterisk in *L*) were also found in the axons of the *dnc-1(RNAi)* worms (*L*). Scale bar = 500 nm (A–C) or 10 μm (D). Statistical analyses were performed using Student's t test (*$p<0.05$ and **$p<0.0001$) and Pearson's correlation coefficient in *H* and *I*. The error bars are S.E.M.
doi:10.1371/journal.pone.0054511.g008

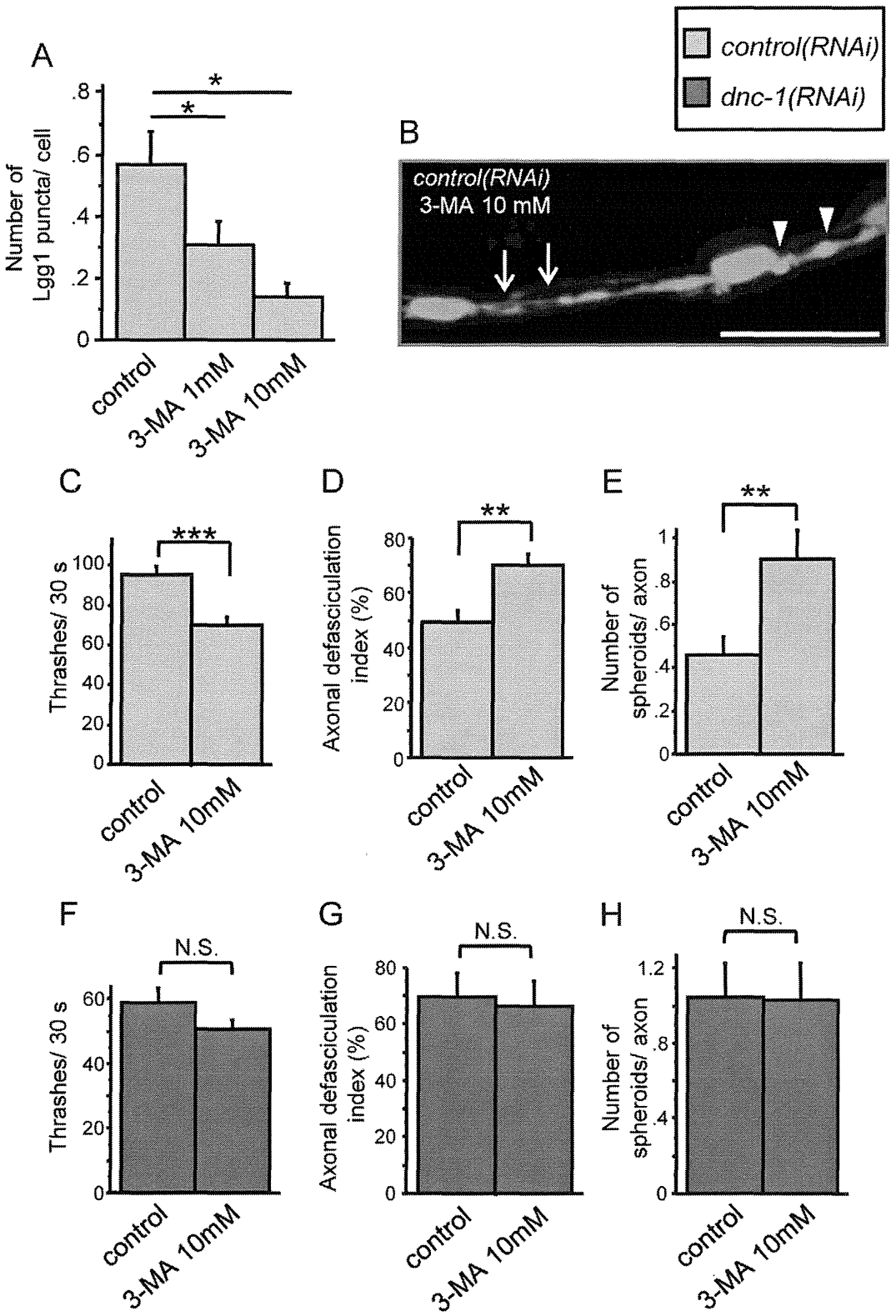

Figure 9. Dysfunction of autophagy causes axonal degeneration. (*A*) Treatment with 3-MA decreased the number of autophagosomes in the ventral nerve cord in a dose dependent manner (n = 15 for each group). (*B–E*) The effects of 3-MA on the locomotor function (*C*) and axonal morphology (*B, D,* and *E*) of the *control(RNAi)* worms. Treatment with 3-MA increased axonal defasciculation (arrows in *B* and the graph in *D*) and the number of axonal spheroids (arrowheads in *B* and the graph in *E*) (n = 15 for each group). (*F–H*) The effects of 3-MA on the locomotor function (*F*) and axonal morphology (*G, H*) of the *dnc-1(RNAi)* worms (n = 15 for each group). Scale bar = 10 μm. Statistical analyses were performed using Dunnett's post hoc test (*A*) and Student's t test (B, *D,* and *E*) (*$p<0.05$, **$p<0.001$, and ***$p<0.0001$). The error bars are S.E.M.
doi:10.1371/journal.pone.0054511.g009

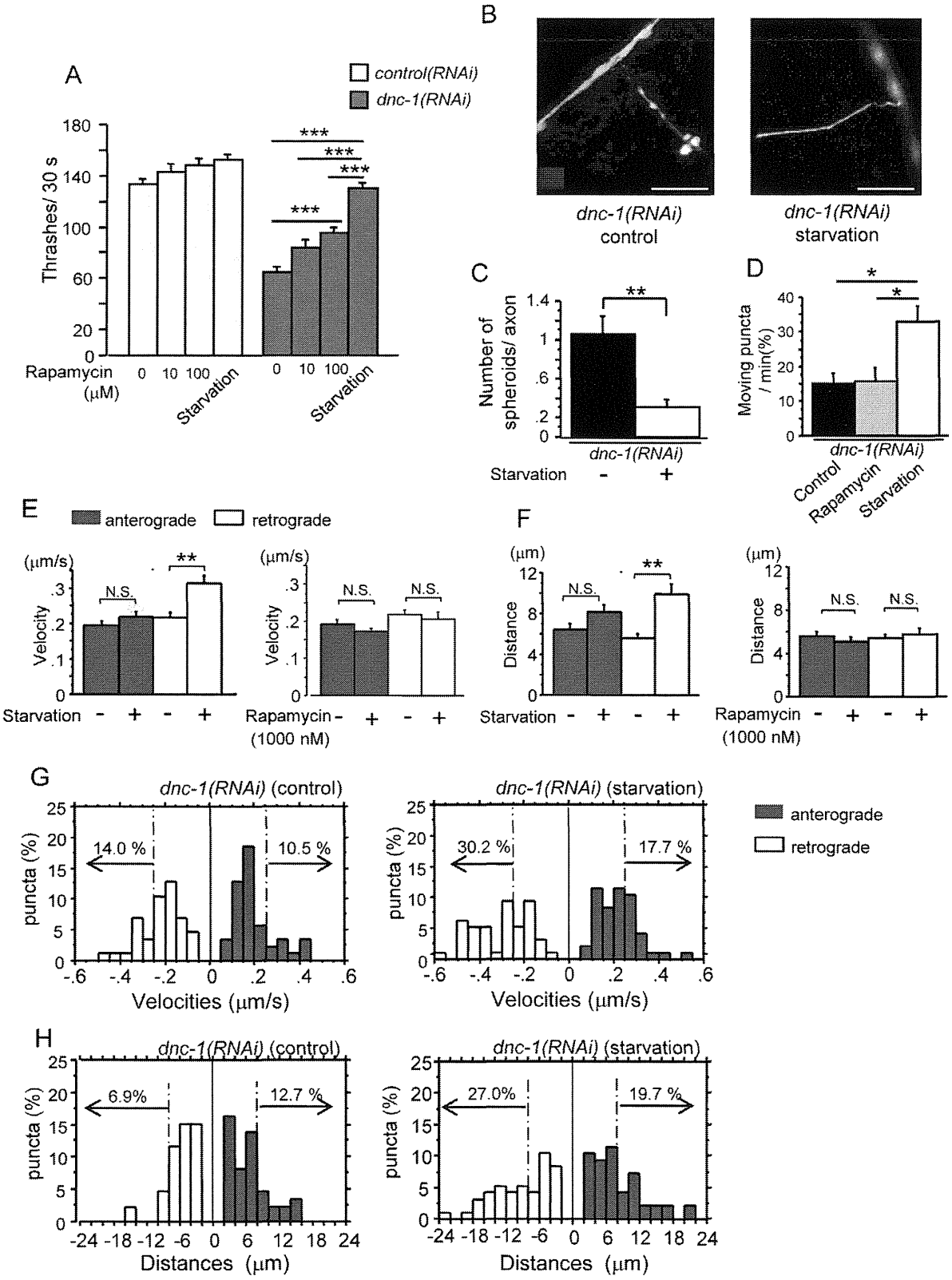

Figure 10. Starvation stimulates the retrograde transport of autophagosomes and attenuates axonal degeneration in the *dnc-1(RNAi)* worms. (*A*) Effect of rapamycin and starvation on locomotor function in the *control(RNAi)* and *dnc-1(RNAi)* worms (n = 50 for each group). (*B*) Fluorescent microscopy showing the morphological changes in axons after starvation in the *dnc-1(RNAi)* worms. (*C*) The number of axonal spheroids per transverse axon section in the *dnc-1(RNAi)* worms with or without starvation. (n = 15 animals for each treatment). (*D*) Effect of rapamycin (100 μM) and starvation on autophagosome mobility in the *dnc-1(RNAi)* worms. (n = 15 animals for each treatment). (*E, F*) Effect of rapamycin (100 μM) and starvation on the mean velocity (*E*) and run-length (*F*) of autophagosomes (black bars: anterograde transport; white bars: retrograde transport) (n = 70

vesicles for each treatment). (*G, H*) Histograms of Lgg1::DsRed velocity (*F*) and run-length (*G*) in the anterograde (black bars) and retrograde (white bars) direction in primary motor neurons from the *dnc-1(RNAi)* worms cultured with normal (control) and serum-free (starvation) medium. Scale bars = 5 μm. Statistical analyses were performed by one-way ANOVA followed by the Bonferroni/Dunn post hoc test (*A*) and Dunnett's post hoc test (*D*). Student's t test (*C*) and Mann-Whitney test (*E, F*) were used for two-group comparison (*$p<0.05$, **$p<0.001$, and ***$p<0.0001$). The error bars are S.E.M.
doi:10.1371/journal.pone.0054511.g010

1–2 frames/s. The images were analyzed using Zen2008 (Zeiss) software. The run-length of Lgg-1 in primary motor neurons was measured by drawing a line over moving fluorescent puncta using Zen2008. Motile puncta were counted only if they moved continuously in the same direction for more than 2 frames and if their displacement was at least 2 μm. Some runs were terminated by a pause or reversal. To ensure the accuracy of the run-length measurements, we excluded moving puncta at the beginning and end of the movie. The velocity of Lgg-1 movements was obtained from the total distance traveled divided by the duration of the run.

***In vivo* transport assay and image analysis.** Time-lapse images were acquired at room temperature using a 63× objective (N.A. 1.4) for live-worm analysis at 1 frame/s. The images were analyzed using Image J 1.43 software (National Institutes of Health). First, individual tracks of SNB-1 or Lgg1 movement were analyzed using the Multiple Kymograph plug-in, as described previously [26]. The velocity of the moving vesicles was tracked manually and their instantaneous velocity was extracted. To calculate the ratio of moving versus total vesicles, the number of vesicles that moved more than 2 μm during each time lapse period was divided with the total number of particles in each acquisition.

Electron microscopy of *C. elegans*. A conventional two-step fixation method was performed as described previously [27]. We provide the detail information in Materials and Methods S1.

Western Blot Analysis and Quantitative real-time PCR. Western blot analyses and quantitative real-time PCR were performed as described previously [28,29]. We provide a detail description in Materials and Methods S1.

Statistical analysis. Statistical analyses were performed using StatView software version 5 (Hulinks, Tokyo, Japan). We used the Kaplan-Meier and log-rank test, Student's t-test, Mann-Whitney U test, and one-way analysis of the variance (ANOVA) with the Bonferroni or Dunnett's post-hoc test. Pearson's correlation coefficient was used to assess the correlation of variables.

Results

Dysregulated dynactin 1 expression and autophagy in degenerated spinal motor neurons in SALS patients

The expression of the *DCTN1* gene was markedly reduced in the spinal motor neurons of SALS patients, as reported previously [9,13] (Fig. 1*A*). Recent studies indicate that the dysregulation of autophagy in motor neurons is a pivotal event in ALS [8,10]; thus, we investigated the relationship between decreased dynactin 1 expression and autophagy in SALS. Immunohistochemistry using consecutive sections of autopsied human spinal cords revealed that LC3 immunoreactivity, a histological marker of autophagy, was increased in the motor neurons of SALS patients in which dynactin 1 expression was decreased (Fig. 1*B*). Conversely, there was no change in the immunoreactivity for dynactin 1 and LC3 in cerebellar Purkinje cells, which showed no degeneration (Fig. 1*C*). Quantitative analysis revealed that anti-LC3 immunoreactivity was significantly increased in the spinal motor neurons of SALS patients ($p<0.0001$) (Fig. 1*D*), and was inversely correlated with the decreased mRNA levels of *DCTN1* (Fig. 1*E*) and cell size (Fig. 1*F*) in the motor neurons of SALS patients, indicating that the dysregulation of autophagy is associated with the decreased expression of dynactin 1 in SALS. Electron microscopy of sections from the SALS and control patients (Fig. 1*G, H*) also revealed that there was an abundance of autophagic vacuoles, e.g., multilamellar bodies (arrowheads in Fig. 1*I, K*), autophagosome-like double membrane vesicles (arrows in Fig. 1*K, J*), and autolysosomes (asterisks in Fig. 1*L*) in the motor neurons of the SALS patients, which were scarcely observed in the control patients.

Generation of the *dnc-1*-depleted *C. elegans* model

To examine the relationship between the loss of dynactin 1, the accumulation of autophagosomes, and motor neuron degeneration, we created a *dnc-1*-KD *C. elegans* model by transfecting *C. elegans* with a plasmid expressing an shRNA and GFP under the control of the motor neuron-specific *acr2* promoter (*dnc-1(RNAi)*). In the transgenic worms, GFP was expressed diffusely in ventral motor neurons (Fig. 2*A*). We confirmed the effect of RNA interference on the level of endogenous *dnc-1* mRNA using whole mount *in situ* hybridization. In the *control(RNAi)* worms, *dnc-1* expression was not altered by *shRNA::GFP* expression (Fig. 2*B*). Conversely, in the *dnc-1(RNAi)* worms, motor neurons expressing *shRNA::GFP* exhibited reduced or no expression of *dnc-1* (Fig. 2*B*). As shown in Fig. 2*C*, approximately 22 neurons were GFP-positive both in the *control(RNAi)* and *dnc-1(RNAi)* worms. The number of *dnc-1*-positive motor neurons was decreased by approximately 20 (*control(RNAi)* worms, 35.3±3.8; *dnc-1(RNAi)* worms, 15.9±9.8), suggesting that *dnc-1* was successfully knocked down in almost all the GFP-positive cells (Fig. 2*C, D*). Moreover, *dnc-1* expression was not affected in the head sensory neurons of the *dnc-1(RNAi)* worms, confirming the specificity of the promoter (Fig. 2*E*). Taking these results into account, in the following experiments, we selected the *dnc-1(RNAi)* and *control(RNAi)* worms expressing GFP in more than 30 motor neurons to avoid the influence of knockdown efficiency on the experimental results.

Motor dysfunction in motor neuron-specific *dnc-1*-KD *C. elegans*

The *dnc-1(RNAi)* worms demonstrated uncoordinated locomotion (Fig. 3*A*), which is a phenotype observed in *C. elegans* mutant models of motor neuronal defects [30,31]. Maturation of the worms resulted in the progressive aggravation of their uncoordinated locomotion, characterized by partial paralysis, slowed movement, and coiling. The feeding plate of the *dnc-1(RNAi)* worms appeared to be stagnated, as they only ate the food around themselves due to their decreased motility (Fig. 3*A*). As described in the Materials and Methods, we generated six lines of *dnc-1(RNAi)* worms: SBG7, 8, and 15 using shRNA1(101), and SBG20, 24, and 25 using shRNA2(2888). Survival analysis and body bend assays were performed using these six lines. Since these animals exhibited almost the same phenotype, SBG8 was employed for further analysis. Compared with the *control(RNAi)* worms, the *dnc-1(RNAi)* worms had a decreased life span (Fig. 3*B, C*) (11.4±4.4, 11.2±3.0, 13.4±4.0, and 14.3±3.3 days for *dnc-1(RNAi-1)*, *dnc-1(RNAi-2)*, *control(RNAi)*, and wild-type worms, respectively). *dnc-1(RNAi)* worms also exhibited significantly reduced bending and thrashing rates that declined with age